Engineered yeast cells simulating CD19+ cancers to control CAR T cell activation

Marcus Deichmann[1], Giovanni Schiesaro[1], Keerthana Ramanathan[2], Katrine Zeeberg[1], Nanna M. T. Koefoed[1], Maria Ormhøj[2], Rasmus U. W. Friis[2], Ryan T. Gill[1,3], Sine R. Hadrup[2], Emil D. Jensen[1]*, Michael K. Jensen[1]*

[1] Novo Nordisk Foundation Center for Biosustainability, Technical University of Denmark, Kgs. Lyngby, Denmark

[2] Department of Health Technology, Technical University of Denmark, Kgs. Lyngby, Denmark.

[3] Artisan Bio, 363 Centennial Parkway, Suite 310, Louisville, Colorado 80027, United States.

* To whom correspondence should be addressed. Emil D. Jensen (E-mail: emdaje@biosustain.dtu.dk) or Michael K. Jensen (E-mail: mije@biosustain.dtu.dk).

Abstract

Chimeric antigen receptor (CAR) T cells have become an established form of immunotherapy and continue to show promising results for the treatment of hematological cancers in most patients. While this immunotherapy continues to generate excitement in the clinic, antigen modulation in cancer cells affects the quality and safety of CAR T cell therapy. Here we present the engineering of yeast to robustly and dynamically modulate antigen densities, hence establishing a novel tool for assessing antigen-density thresholds in CAR T cell responses. Using a synthetic biology approach, we successfully engineer yeast to simulate cancer cells and demonstrate i) controllable antigen densities of CD19 through the use of G protein-coupled receptors (GPCRs), ii) a customizable system for tuning antigen densities through the employment of heterologous GPCRs for defining signal input types and signal pathway engineering for adapting intensities, and iii) activational control of clinically-derived CAR T cells within a physiologically relevant range compared to the activation elicited by a NALM6 cancer cell line. Based on this yeast-based antigen-presenting cell system, we envision an efficient assessment of how varying antigen densities in cancer cells from patients affect CAR T cell responses and ultimately support safer and better quality of personalized cancer therapies.

Introduction

During the last two decades, synthetic biology has paved the way for the development of genetically engineered cells equipped with programmable gene circuits to control the onset and intensity of therapeutic functions in response to specific inputs, thereby fostering novel clinically relevant abilities in both microbes and human cells [1]. Simultaneously, cellular immunotherapies have evolved to show promising clinical results for the treatment of cancers [2]. At the interface between these rapidly advancing fields lies chimeric antigen receptor (CAR) technology, which commonly relies on engineered autologous T cells to heterologously express a synthetic CAR construct enabling T cell anticancer responses upon patient re-infusion. Currently applied 2nd generation CARs are modular and customizable, containing an extracellular binding domain for recognizing a cancer cell-surface antigen (e.g. CD19), a structural hinge, as well as a transmembrane domain connecting external cues to intracellular signaling domains, providing co-stimulation (e.g. CD28 or 4-1BB) and ultimately T cell activation (CD3ζ) [3–6]. Since 2017, six FDA approvals on the use of CARs for hematological cancers have been registered [5]. These include anti-CD19 CAR T cells for relapsed or refractory (r/r) B cell acute lymphoblastic leukemia (B-ALL) with clinical trials and real-world studies showing complete remission (CR) in 70-96% of patients [7–16].

However, while remission rates are encouraging, 14-57% of r/r B-ALL patients obtaining CR from anti-CD19 CAR T cell immunotherapy eventually experience relapse [7–16]. Indeed, the field of CAR T is still emerging, and major challenges need to be mitigated to further improve their safety and efficacy, including mitigation of inhibitory immunosuppression, severe toxicity, CAR T cell trafficking, and target antigen escape [5,6,17]. While some relapses are caused by immunosuppression, exhaustion, or poorly persistent and ineffectual CAR T cells [16,18–20], others are attributed directly to escape by cancer cell antigen modulation, where CAR T cells may remain functional, but simply lack a targetable antigen [21]. Such antigen modulation is hypothesized to be a major factor in determining response durability and the dominant mechanism of tumor escape in r/r B-ALL [5,6], occurring in 7-28% of r/r B-ALL CRs and being associated with poor prognosis [7–12,15,16,22–24].

CD19 modulation reshapes the patients' total antigen burden and can occur through a variety of mechanisms [21,25–32]. Regardless of the targeted antigen, even a gradual decrease in antigen density alone provides a mechanism of reduced efficiency and increased resistance to CAR T cell therapy [32–41]. These antigen density-dependent effects have differential impact across CAR designs and CAR expression levels [32–34,37,38,40,41]. Resistance is not the only challenge imposed, since antigen densities also modulate the efficiency of CAR T cells, as various abilities that are needed to support the anticancer response are triggered at different threshold antigen density levels with different intensities. For instance, it has been reported that cytolytic activity requires a lower antigen density

than CAR T cell proliferation and release of cytokines [33–36,38,39]. However, the exact impact of CD19 density on CAR T cell efficiency is unclear, and there seems to be a fine line between therapeutic and adverse or toxic effects. Specifically, CAR activation is required for efficient anticancer responses, yet, too rapid and excessive CAR T cell activation can induce extensive systemic inflammatory immune responses leading to serious toxic adverse events [42]. Such acute toxicity is common in r/r B-ALL therapy, with cytokine release syndrome (CRS) reported to occur in 77-100% of patients and immune cell-associated neurotoxicity syndrome (ICANS) in 29-50% of patients, both of which are potentially life-threatening [7–12,22,24,42,43]. Differential antigen density, and modulation hereof, is also known to increase the complexity of distinction between healthy and cancerous cells, which is associated with on-target, off-tumor toxicity [44]. Furthermore, higher patient-specific tumor burden, and hence the associated total antigen burden, is more often correlated with lower CR and higher *in vivo* post-infusion CAR T cell activation, expansion, cytokine release, and consequently increased risk and severity of CRS and ICANS [7,8,10,42,43,45,46]. Similar issues occur for high CAR T cell doses [42,43,46], although high initial peak circulating CAR T cell levels are associated with durable responses [5], emphasizing that perturbations in effector-to-target cell ratios affect the efficiency and safety profile of CAR T cell therapy.

Despite the clinical importance of understanding antigen densities and the hundreds of new CAR designs and therapies for new target antigens and cancers being developed or undergoing clinical trials [47], only a few options exist to assess antigen-density thresholds for CAR T cell responses, such as material-fixed antigens or antigen multimers [41,48,49]. Additionally, cell lines with varying antigen densities, which more closely imitate *in vivo* cell-to-cell interactions, are also used, albeit with a lack of orthogonality and limited control of antigen densities [32–40,50,51]. Here we show that yeast synthetic biology offers a novel platform solution to address this shortcoming by enabling robust, tunable, orthogonal, and CAR-specific methods for controlled simulation of antigen densities in engineered yeast cells directly interacting with human immune cells.

Results

Designing a cancer-simulating yeast cell

In the interest of establishing a novel platform technology for evaluating antigen-density thresholds for immune cell responses, we initially aimed to develop artificial cancer-simulating CD19+ cells from baker's yeast *Saccharomyces cerevisiae*, for orthogonal and controllable *ex vivo* activation of human CAR T cells targeted against the antigen CD19. Several main features were considered key to establishing a whole-cell platform technology for such interspecies cellular communication. First, controllability of antigen density (output) on yeast cells in relation to sensory stimuli (input). Second,

tunability in regards to maximization of output dynamics, and the ability to fine-tune signal transduction. Third, orthogonality in regards to minimizing unintentional immune cell responses and maintaining full system control. Lastly, customizability in terms of choice of input and output signal allows for modularity and adaptation to user-defined cell assays. To fulfill these criteria, we sought to devise engineered G protein-coupled receptor (GPCR) biosensors, converting extracellular input in the form of GPCR ligands into MAP kinase-amplified intracellular signals through the well-characterized and highly modular signaling cascade of the *S. cerevisiae* pheromone response pathway (PRP), known to elicit dynamically regulated expression outputs [52–56]. From this, we were interested in combining such a biosensing technology with yeast surface display (YSD) to provide a controlled CD19 presentation output [57–59]. Hence, creating a novel Synthetic Cellular Advanced Signal Adapter (SCASA) system, the yeast cells would be engineered to display CD19 on the cell surface (*effector module*) at an intensity proportional to the intracellular signal transduced (*processing module*) from a sensed amount of a given extracellular GPCR ligand presented to the cells (*sensory module*) (**Fig. 1A**). Taken together, the establishment of such a SCASA system was hypothesized to enable the simulation of cancer cell heterogeneity through controlled variation in heterologous expression of surface antigen and accordingly be used to assess clinically relevant questions related to antigen-density thresholds for CAR T cell responses (**Fig. 1B**).

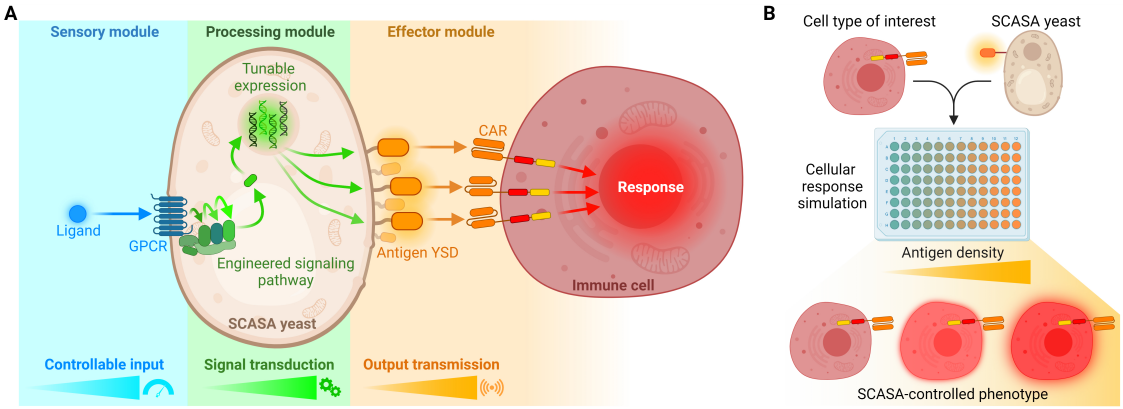

Figure 1. **Outline of the Synthetic Cellular Advanced Signal Adapter (SCASA) system**. **A.** SCASA yeast cells engineered to present tunable dosages of antigens via yeast surface display (YSD) on the cell surface (*effector module*), proportional to the intracellular signal transduced via an engineered pheromone response pathway (*processing module*) with controlled activation and intensity by G protein-coupled receptors (GPCRs) based on cognate ligands presented to the cells (*sensory module*). Each module is customizable to adapt to the specific application of the SCASA yeast cells. **B.** Exemplification of a co-cultivation layout in which engineered SCASA yeast cells are used to simulate different antigen densities of a CAR T cell target to obtain gradual intensities of CAR T cell responses.

Characterization of SCASA processing modules

In order to generate a collection of well-characterized modular processing parts for tuning output intensity (e.g. CD19), candidate promoters for controlling regulation of effector module expression cassettes were selected based on our recent transcriptome analysis of differentially expressed genes linked to GPCR-mediated PRP activation (**Fig. 2A**) [52]. From this, we selected 11 native promoters with different expression characteristics, ranging from undetectable basal mRNA levels to the most highly expressed gene in *S. cerevisiae*, and spanning 6 orders of magnitude in differential mRNA abundance across GPCR stimulation levels, including genes regulated by the commonly used PRP-regulated promoters P_{FUS1} and P_{FIG1} (**Suppl. Fig. 1, Suppl. Table 1**) [60]. To characterize expression from different processing modules (i.e. the transduced intracellular signal), yEGFP-expression cassettes controlled by each promoter were genomically integrated into an optimized GPCR-biosensor strain [53], relying on the yeast mating GPCR Ste2 (strain DIX14). Each resulting strain was analyzed by flow cytometry after exposure to a 10-fold dilution series of the Ste2 ligand α-factor (0-100 µM) (**Fig. 2**).

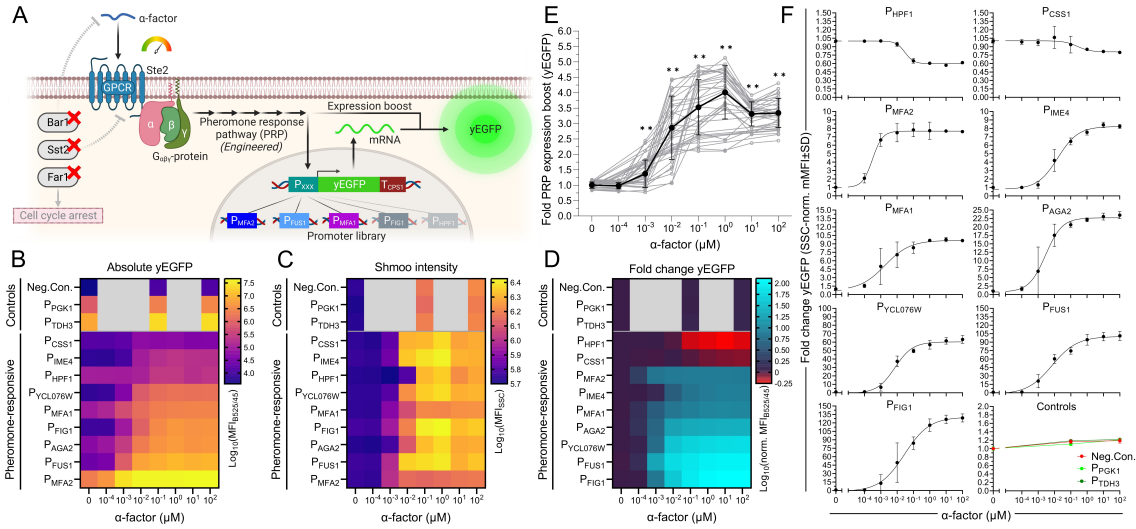

Figure 2. Characterization of the system processing module: promoters and PRP-induced expression boost. A. Strains genetically optimized for GPCR-biosensing by overexpression of GPCR Ste2 and Gpa1, which is the G_{α}-subunit of the heterotrimeric $G_{\alpha\beta\gamma}$-protein that couples GPCRs to the pheromone response pathway (PRP). Additionally, several native genes were knocked out: *ste2Δ0*, *ste3Δ0*, *gpa1Δ0*, *sst2Δ0*, *bar1Δ0*, and *far1Δ0*. A PRP-induced boost post-transcriptionally amplifies the expression of genes. Several PRP-regulated promoters were characterized for the processing module using yEGFP: P_{MFA2}, P_{FUS1}, P_{AGA2}, P_{FIG1}, P_{MFA1}, $P_{YCL076W}$, P_{HPF1}, P_{IME4}, and P_{CSS1}, as well as two constitutive promoters: P_{TDH3} and P_{PGK1}. A negative control without a yEGFP expression cassette was also included. **B.** Absolute yEGFP levels (log_{10}-scale) of designs employing the individual promoters, including effects of the PRP expression boost, quantified by flow cytometry (B525/45) after GPCR stimulation across a 10-fold dilution series of α-factor (0-100 µM). The promoters are sorted on maximum absolute yEGFP intensity, from low to high. **C**. Intensity of PRP-regulated morphological changes (shmooing) of cells as a measure of PRP activation (log_{10}-scale), quantified by flow cytometry (SSC). The promoters are sorted on maximum absolute yEGFP intensity, from low to high. **D**. Fold change induction of promoters (log_{10}-scale), excluding the PRP boost (SSC-

normalized). Promoters are sorted on fold change, from low to high. **E**. Approximated general PRP-induced expression boost from quantified PRP activation (*black*) across all strains and designs (*grey*). **F**. Fold changes of individual promoters, excluding PRP boost (SSC-normalized), with curve fitting using variable slope (four-parameter) nonlinear regression. Data represents means of median fluorescence intensity (mMFI) for biological replicates (n=3, except for E where n=27) and standard deviations hereof. Significance levels: * P≤0.01, ** P≤0.0001. Not all pairwise comparisons are shown. Statistics and extended analyses in: **Suppl. Fig. 1-5** and **Suppl. Table 1-4**.

Following GPCR stimulation all designs displayed significant ligand concentration-dependent changes in yEGFP expression with diverse intensities, highly dependent on the choice of processing module promoter (**Fig. 2B**). In fact, across all promoters and stimulation levels, the variation in yEGFP expression was attributed mainly to the choice of promoter (SV=75.2%), rather than the stimulation level of the GPCR (SV=13.4%)(**Fig. 2B, Suppl. Table 2**), emphasizing the impact of promoter choice on the output. For example, compared to all other promoters, P_{MFA2} showed the highest maximum intensity (p≤0.0138) (**Fig. 2B**), as well as the largest range in absolute output intensity (p≤0.0348) (**Suppl. Fig. 2**). In comparison to P_{TDH3}, which is commonly regarded as the strongest constitutive yeast promoter [61], P_{MFA2} had 0.30±0.04-fold the intensity in the absence of PRP activation, whilst at maximum PRP activation (100 µM) P_{MFA2} enabled 6.7±0.8-fold higher intensity than baseline P_{TDH3} expression (**Fig. 2B**). In regards to maximum absolute reporter intensities, P_{MFA2} was followed by P_{TDH3}, P_{FUS1}, P_{AGA2}, P_{FIG1}, P_{PGK1} P_{MFA1}, and $P_{YCL076W}$, and finally P_{HPF1}, P_{IME4}, and P_{CSS1}, altogether spanning 6,866-fold in total library range with PRP activation (0-100 µM) and 1,025-fold in basal levels (0 µM) (**Fig. 2B**).

We discovered that tuning of the output intensity was not only dependent on the choice of processing module promoter, but also PRP-controlled phenotypical changes of the engineered yeast. Shmooing, a morphological key indicator of PRP activation measured as cellular complexity [52], was most intense at ≥0.01 µM, and generally peaking at 1 µM across all strains (**Fig. 2C**). The effect was mainly attributed to the ligand concentration (SV=84.4%) with little variation between strain designs (SV=3.9%)(**Suppl. Table 2**), indicating similar PRP activation across strains. Interestingly, we discovered that PRP activation causes a general amplification of gene expression, as we observed increased yEGFP levels in response to GPCR stimulation for P_{PGK1} and P_{TDH3} (**Fig. 2B**), despite showing no up-regulation of mRNA levels (**Suppl. Fig. 1**, **Suppl. Table 1**) and being commonly regarded as constitutive [52,61]. We determined that this PRP-induced boost amplifies gene expression multiplicatively from any promoter in yeast post-transcriptionally with an intensity that is PRP-stimulation-dependent (p<0.0001)(**Fig. 2E**, **Suppl. Fig. 3**), and is part of the phenotypic changes occurring during yeast mating, as well as being fully dependent on Ste12, the main transcription factor of the PRP [60] (p<0.0001)(**Suppl. Fig. 4**). We estimate that the PRP boost amplified yEGFP expression by 4.0±0.9-fold across all designs following 5

hrs of GPCR stimulation (**Fig. 2E**), emphasizing a significant contribution of the PRP-mediated phenotypic remodeling of yeast cells to the output of SCASA yeast cells.

We obtained different absolute yEGFP expression profiles from processing modules in combination with the PRP boost (**Fig. 2B**), such as the strongest promoter P_{MFA2} showing a 20.3±1.3-fold up-regulation, and the promoter with highest dynamic range, P_{FIG1}, peaking with a maximum fold change of 516.8±83.0 (**Suppl. Fig. 5**). Upon isolation of promoter response kinetics from the PRP boost, fold changes ranged from 128.8±7.2-fold (P_{FIG1}) to 0.62±0.01-fold (P_{HPF1}), thus revealing both up- and down-regulation of system signaling (**Fig. 2F**). Interestingly, promoters P_{HPF1} and P_{CSS1} showed down-regulation upon PRP stimulation and displayed inverse agonist behavior (**Fig. 2F**), supported by decreasing mRNA levels of the cognate genes (**Suppl. Fig. 1**, **Suppl. Table 1**).

In summary, our results highlight a SCASA processing module relying on two separate sequential events contributing to the control of gene expression via PRP-coupled GPCR sensory inputs, as demonstrated for 11 promoters. Firstly, a transcriptional response of PRP-regulated promoters with diverse basal activities and tunable dynamic output ranges, in accordance with previous studies [53,60,62], and secondly, a post-transcriptional PRP boost caused by phenotypic changes to the yeast cell.

Modules for dynamic regulation of CD19 yeast surface display

To further develop SCASA, we next sought to devise an effector module for the dynamic regulation of surface CD19 as a system output. For YSD, a highly mutated CD19 extracellular domain (CD19.1 ECD) was employed for correct folding and expression in yeast [57,58], hereafter merely denoted CD19. The display construct is a fusion of a hemagglutinin (HA) tag, a PAS40-linker, a $(G_4S)_3$-linker, and CD19, to the C-terminal of Aga2, also containing the native N-terminal Aga2 signal peptide (**Fig. 3A**).

Here, YSD and folding of functional CD19 were first confirmed in all yeast strains via staining with FMC63-clone anti-CD19 antibody containing the binding domain of current FDA-approved CAR T cell designs (**Fig. 3**) [5]. Specifically, effector modules of genome-integrated cassettes for constitutive expression efficiently allowed CD19 display with 99.7±0.3% CD19+ yeast cells, thus closely resembling the phenotype of the cancer benchmark CD19+ NALM6 B cell leukemia cell line (100±0% CD19+)(**Fig. 3B**).

For the simulation of specific immune and cancer cell interactions, a controlled homogenous response is desired for delivering a signal of specific intensity to receiver cells (e.g. CD19). However, conventional methods for YSD often result in heterogeneous population behavior, seen as multimodal display distributions within a single culture, driving us and others away from conventional YSD systems to improve display efficiencies [63–66]. We verified the lower efficiency of the traditional EBY100 strain with pCT-plasmid-based YSD [59,67] using galactose-induced expression of CD19 from P_{GAL1} resulting in

only 38.6% CD19+ yeast cells (**Fig. 3B**). Our further analyses largely attributes the heterogeneity of conventional YSD to, firstly, the common use of plasmid-based expression and, secondly, the binary response kinetics of P_{GAL1} that can not be titrated by gradual galactose supplementation homogeneously at the single-cell level (**Suppl. Fig. 6**). Genome integration resolved the issue of plasmid-related heterogeneity, improving the maximum of CD19+ cells from 41.2±6.4% to 99.2±0.2%, however, due to the limits of P_{GAL1}-response kinetics, this was restricted to only maximal galactose induction (**Suppl. Fig. 6**). Hence, we concluded that conventional YSD methods were unfit for dynamic control of high-precision cellular communication.

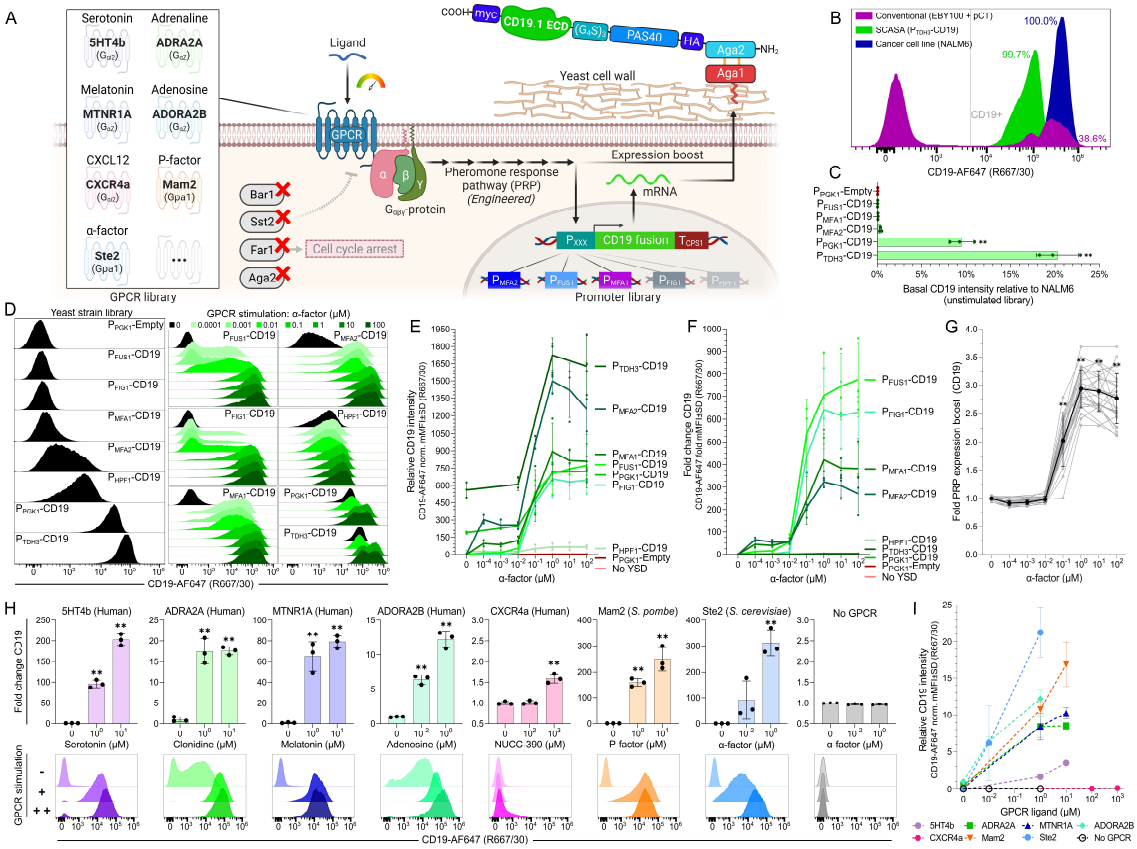

Figure 3. **Characterization of SCASA system tunable CD19 antigen presentation by yeast cells. A.** Illustration of the characterized designs of SCASA yeast cells for controllable CD19 densities. The yeast surface display (YSD) construct enabling a CD19 effector output is composed of a fusion protein of a hemagglutinin (HA) tag, a PAS40-linker, a $(G_4S)_3$-linker, and CD19.1 ECD, fused to the Aga2 C-terminal, employing the native N-terminal Aga2 signal peptide. The expression intensity of CD19 was regulated by processing modules based on the promoter library (**Fig. 2**). A library of heterologous GPCRs with various ligand types was employed to customize the sensory input controlling CD19 expression. In addition to the genetic optimization of the system described in **Fig. 2**, native Aga2 was knocked out (*aga2Δ0*) and anchor protein Aga1 overexpressed. **B.** Comparison of system performance to cancer cell expression of CD19. Conventional YSD of CD19 was assessed using the traditional EBY100 strain containing a pCT-type plasmid with galactose-inducible (P_{GAL1}) CD19 expression (2%Gal, 24 hrs.). The SCASA yeast cell design expressed CD19 constitutively via P_{TDH3} from a genome-integrated cassette. The human CD19+ NALM6 B cell leukemia cell line was included as a benchmark control. The percentage of alive CD19+ cells is

provided. **C**. Basal CD19 density of SCASA yeast strains from the processing module library relative to NALM6 (100%) without stimulation of their GPCRs. **D.** CD19 display of the SCASA yeast processing module library with different promoters, without any GPCR stimulation (*black*) and with GPCR stimulation (Ste2) across a 10-fold dilution series of α-factor (0-100 µM) (*green*). **E.** Comparison of quantified CD19 display levels during GPCR stimulation of the SCASA yeast processing module library, normalized to the lowest detected CD19 level. 'No YSD' denotes background strain DIX41. **F**. Comparison of fold changes of CD19 display levels during GPCR stimulation of the SCASA yeast processing module library. **G**. Approximated general PRP-induced expression boost of CD19 from quantified PRP activation (*black*) across all strains and designs in the yeast processing module library (*grey*). **H**. Characterization of heterologously expressed human and fungal GPCRs for controlling CD19 densities using alternative ligands and agonists. All strains employ the P_{FUS1} processing module and only vary in the type of GPCR and G_{α}-subunit. The top row shows the fold change in CD19 levels in response to GPCR stimulation, and the lower row shows the populational behavior. **I.** Comparison of quantified CD19 display levels for the different GPCRs across stimulation using cognate ligands or agonists. PRP activation and CD19 levels were quantified by flow cytometry. Data is based on means of cell counts or median fluorescence intensities (mMFI) for biological replicates (n=3, except for G where n=15) and standard deviations hereof. Histograms are normalized to the unit area (B) or mode (D+H) and are representative replicates. Significance levels: * P≤0.01, ** P≤0.0001. Not all pairwise comparisons are shown. Statistics and extended analyses in: **Suppl. Fig. 6-8** and **Suppl. Table 5-6**.

To build controllable and customizable YSD systems enabling tunable intensity at the single-cell level with homogenous population behavior, we therefore went for fully genome-integrated GPCR-based inducible systems (**Fig. 3A**). Here, CD19-expression cassettes were generated using chosen processing modules previously characterized; P_{MFA2}, P_{FUS1}, P_{FIG1}, P_{MFA1}, P_{HPF1}, P_{TDH3}, and P_{PGK1} (**Fig. 2**). Cassettes were genome-integrated in the GPCR-biosensor strain with further optimization of YSD capabilities by overexpression of YSD anchor Aga1 and deletion of native *AGA2* (*aga2Δ0*) to avoid potential competitive binding to Aga1 (strain DIX41) (**Fig. 3A**). We also generated a negative control strain with P_{PGK1}-controlled display of an Aga2-fusion protein lacking the CD19 coding sequence (P_{PGK1}-Empty). Default expression levels of processing module promoters enabled the generation of a library of strains with different constitutive CD19 densities, simulating cancer cells with different CD19 levels. Specifically, the unstimulated P_{TDH3} yeast design had a CD19 level 20.3±2.4% of NALM6, followed by P_{PGK1} at 9.5±1.4%, and P_{MFA2} at 0.4±0.1% (**Fig. 3C**). At unstimulated conditions, P_{TDH3}, P_{PGK1}, P_{HFP1}, and P_{MFA2} provided distinct basal CD19 densities (p<0.0001), while P_{FIG1} and P_{FUS1} provided undetectable levels of CD19 (**Fig. 3D**), yielding an overall span in CD19 levels of the unstimulated library of 562-fold (**Fig. 3E**).

We next pursued tunable CD19 antigen densities via GPCR stimulation, by exposing the strains to a 10-fold dilution series of α-factor (0-100 µM), providing a multitude of different CD19+ profiles (**Fig. 3D-F**). Importantly, for all library strains, CD19 density could be significantly diversified from their default levels through stimulation of the GPCR (p<0.0001)(**Fig. 3D-F**). Specifically, the highest acquired CD19 antigen density was obtained for P_{TDH3} at 1,724±151-fold and P_{MFA2} at 1,498±96-fold the lowest basal CD19 level (p≤0.0001)(**Fig. 3E**), while the largest span in absolute CD19 antigen density relative

to the unstimulated condition was seen for P_{MFA2} ($p \leq 0.0361$)(**Suppl. Fig. 7**), all at 1 µM α-factor. P_{MFA1}, P_{FUS1}, P_{PGK1}, and P_{FIG1} provided similar intermediate output profiles at >0.1 µM α-factor, while P_{HPF1} only provided modest levels of CD19 (**Fig. 3E**). Importantly, fold changes in CD19 levels revealed that P_{FUS1}, P_{FIG1}, P_{MFA1}, and P_{MFA2} could all provide drastic changes in CD19 display relative to the unstimulated condition ($p<0.0001$) (**Fig. 3F**), with P_{FUS1} (774±165-fold) and P_{FIG1} (630±99-fold) providing up-regulation from undetectable CD19 to levels comparable to P_{TDH3} (**Fig. 3E-F**), highlighting that these individual strains were capable of spanning the entire CD19 density range provided by the unstimulated strain library (**Fig. 3D-F**).

All strains showed shmooing coinciding with a CD19 expression boost at ≥0.1 µM α-factor ($p<0.0001$), with an estimated maximum PRP boost effect of 2.9±0.3-fold at 1 µM after 20 hrs (**Fig. 3G**), which was attributed to GPCR stimulation (SV=94.7%) and not to strain design differences (SV=0.9%)(**Suppl. Table 5**). Remarkably, the importance of the seemingly modest PRP boost should not be neglected, as the change of absolute output from the 3.1±0.3-fold up-regulation of P_{TDH3} was greater than the 774±165-fold up-regulation of P_{FUS1} (150.2±37.5%, $p=0.012$) (**Suppl. Fig. 7**), hence allowing high-intensity antigen presentation, extreme changes in signal output, and larger diversity in the library.

In summary, CD19 antigen density was controllable on SCASA yeast cells, enabling the generation of CD19 density profiles spanning 1,724-fold in intensity across the library, via seven different processing module promoters constituting a basal library that was modifiable through GPCR stimulation. Importantly, the response control for CD19 density was continuous (non-binary), dependent on the GPCR ligand concentration, specific for the individual processing module, and showed no distinct residual non-displaying populations, across the different levels of stimulation (**Fig. 3D-G**).

Coupling of heterologous GPCRs allows for a customized sensory module

One important component of engineered living systems is the ability to create sense-response functions that can accommodate different input signals [1]. In order to make a yeast-based SCASA cell that can employ different ligands as controlling inputs, we assessed whether our sensory module could comprise different heterologously expressed GPCRs. Naturally, GPCRs allow for concentration-dependent signal transduction to provide outputs of regulated intensity, and display exceptional diversity to sense various types of ligands, ranging from light rays and small molecules to peptides and larger complex proteins [53,56,68,69]. Genes encoding GPCRs MTNR1A[53], ADORA2B[53], ADRA2A[54], 5HT4b[70], Mam2[53], and CXCR4a[71] were chosen accordingly, and individually heterologously expressed and coupled to either native Gpa1 or the chimeric $G_{\alpha Z}$ or $G_{\alpha i1/2}$-subunits in the optimized background strain

employing display of CD19 from P_{FUS1} (strains DIX57-58). The constructed GPCR library covered sensing of small molecules (melatonin, adenosine, adrenaline, serotonin), peptides (P-factor), and complex proteins (CXCL12/SDF-1)(**Fig. 3A**). All GPCRs were functional and showed significant up-regulation of CD19 surface levels upon stimulation with their cognate ligands or agonists ($p<0.0001$)(**Fig. 3H**). GPCR expression caused significantly different background levels of CD19, with the lowest being 5HT4b, even lower than the no GPCR control ($p<0.0001$), and at 58.8±5.4-fold higher, ADORA2B caused the highest unstimulated CD19 level ($p\leq0.0013$) (**Fig. 3H-I**). In the tested operational ranges, the highest absolute CD19 levels and fold changes were provided by fungal peptide-sensing GPCRs Ste2 (312.5±50.0-fold) and Mam2 (249.4±50.0-fold)(**Fig. 3H**), while GPCRs sensing human neurotransmitters showed slightly lower absolute CD19 levels (**Fig. 3I**), as well as different fold changes; 5HT4b (202.6±13.8-fold), MTNR1A (79.2±5.9-fold), ADRA2A (17.6±0.9-fold), and ADORA2B (12.2±1.2-fold)(**Fig. 3H**). The human chemokine-sensing CXCR4a showed a modest 1.6±0.1-fold up-regulation of CD19 levels (**Fig. 3H**). The different GPCRs enabled varying degrees of general PRP activation, with all but CXCR4a showing significant phenotypic changes ($p\leq0.0003$)(**Suppl. Fig. 8**).

In summary, the sensory module was customizable, exemplified by the expression of six exogenous heterologous GPCRs enabling the adoption of small molecule-, peptide-, and protein-based input signals, and providing a 1,249-fold span in CD19 densities across the examined range of GPCR stimulation.

Co-cultivation of yeast and human T cells

Before proceeding to yeast-mediated CAR T cell activation assays, it was critical to assess the basic physiological properties of co-cultivation of the engineered yeast with human immune cells. For this purpose, we first established that yeast showed negligible growth in T cell media, RPMI+10%FBS and ImmunoCult™-XF T Cell Expansion Medium, not initiating growth for at least 22 hrs, providing stable yeast cell numbers during co-cultivation, and preventing that yeast could overtake cultures (**Suppl. Fig. 9**). Secondly, we co-cultivated yeast with donor-derived naïve T cells at cellular ratios of 0.5x, 1.0x, and 10x yeast cells with compliance to T cell growth requirements for 96 hrs, at which T cell viability and proliferation was not affected by the presence of yeast at any ratio (**Suppl. Fig. 9**). Lastly, we verified that the SCASA system of the engineered yeast cells remained functional during T cell growth conditions, despite the constrained growth in T cell media (**Suppl. Fig. 9**).

In summary, all experiments indicated that yeast and T cell co-cultures were possible under standard T cell growth requirements without affecting the viability or inducing proliferation in donor-derived naïve T cells, and with yeast cells showing constrained growth but retaining functionality.

Controlled human immune cell activation by SCASA yeast cells

After construction and characterization of the controllable CD19-presenting SCASA yeast cells, and verifying co-cultivation with human cells, we proceeded to validate their ability to communicate with immune cells of relevance to immuno-oncological applications. Here, a Jurkat cell line equipped with a nuclear factor of activated T cell (NFAT) transcription factor luciferase reporter system (Jurkat NFAT-Luc) was transduced with lentiviral vectors to express an anti-CD19 CAR (FMC63-CD8α-4-1BB-CD3ζ) [72], thus enabling a bioluminescent signal of an intensity proportional to the CAR T cell activation level imposed by the CD19+ SCASA yeast cells (**Fig. 4A**).

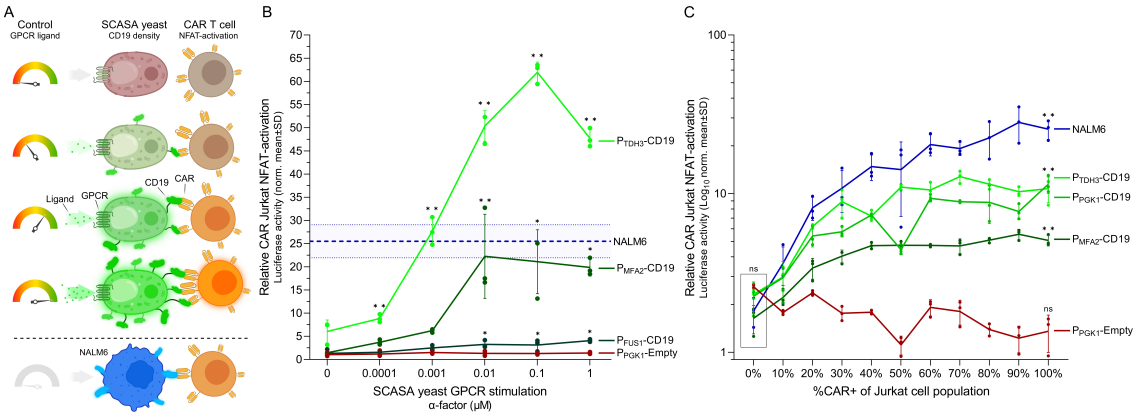

Figure 4. Activation of CAR Jurkat NFAT-Luc cells using SCASA yeast cells. A. Representative illustration of co-culture of Jurkat cells and SCASA yeast cells. The Jurkat cells that express anti-CD19 CARs (CAR+) bind to the surface of SCASA yeast cells that display CD19, analogously to as seen for NALM6. The Jurkat cells contain a nuclear factor of activated T cells (NFAT) transcription factor luciferase reporter system (NFAT-Luc), which upon CAR activation express luciferase. The SCASA yeast cells have the possibility to be stimulated through their GPCRs, in this case, Ste2 with ligand α-factor, to induce differential CD19 antigen density. **B.** Co-cultures of 100% CAR+ Jurkat NFAT-Luc cells with three different SCASA yeast designs (P_{FUS1}-CD19, P_{MFA2}-CD19, and P_{TDH3}-CD19, *green lines*), with and without α-factor stimulation (0-1 μM) of the SCASA yeast cell GPCR, Ste2. As a negative control, we used yeast lacking the CD19 CDS in the display construct (P_{PGK1}-Empty, *red line*). Before co-cultivation, the individual SCASA yeast cells were stimulated with α-factor for 20 hrs to induce controlled increase in the CD19 surface display. As a positive benchmark control, the activation level provided by CD19+ human cancer cell line NALM6 is plotted (*blue line*) **C**. Co-cultures of Jurkat NFAT-Luc cells with three different SCASA yeast designs; P_{MFA2}-CD19, P_{PGK1}-CD19, and P_{TDH3}-CD19, as well as a negative control P_{PGK1}-Empty, and NALM6 as benchmark control. The percentage of Jurkat NFAT-Luc cells in the co-culture expressing CARs was graded from 0-100% CAR+. Data is based on means of three biological replicates (n=3) and standard deviations hereof. Significance levels: * P≤0.01, ** P≤0.0001. Not all pairwise comparisons are shown. Statistics and extended analyses in: **Suppl. Fig. 10** and **Suppl. Table 8.**

To demonstrate controllable synthetic cell-to-cell communication, we initially diversified the antigen densities of CD19+ SCASA yeast cells to simulate cancer cells with varying CD19 levels by controlled stimulation of their GPCRs. To do so, we stimulated the Ste2 receptor with 0-1 μM α-factor, and co-cultivated them with 100% CAR+ Jurkat NFAT-Luc cells (**Fig. 4A**). Upon GPCR stimulation, all CD19+ yeast designs could significantly induce differential and gradual activation of CAR+ Jurkat cells

($p \leq 0.0045$)(**Fig. 4B**). Different yeast designs induced distinct maximal activation intensities throughout their controlled CD19 densities. The most intense was enabled by the P_{TDH3}-CD19 design yielding 61.9±2.2-fold increased NFAT activity relative to a control mono-culture of 100% CAR+ Jurkat cells (0.1 µM, $p<0.0001$). This was followed by the P_{MFA2}-CD19 design at 22.3±9.1-fold NFAT activity (0.01 µM, $p=0.0007$), and the P_{FUS1}-CD19 design at 4.1±0.3-fold (1 µM, $p=0.0026$)(**Fig. 4B**). Importantly, these values correlate with the order of SCASA yeast CD19 densities (**Fig. 3E-F**), and further demonstrated that CD19+ SCASA yeast cells with the P_{TDH3}-CD19 design could exceed the CAR Jurkat cell activation intensity elicited by the benchmark NALM6 cancer cell line by 2.4±0.4-fold ($p<0.0001$) (**Fig. 4B**).

The CAR employed in this experiment made use of the 4-1BB costimulatory domain, which has been associated with a higher CD19 antigen-density threshold of activation, making the CAR T cells less reactive to low CD19 densities [38]. SCASA yeast cells with processing modules of high background CD19 levels (e.g. P_{TDH3}-CD19) provided higher activation sensitivity, as they reached the threshold of efficient FMC63-CD8α-4-1BB-CD3ζ CAR activation at significantly lower levels of GPCR stimulation than the other designs (**Fig. 4B**). Similarly, a high dynamic range of CAR activation relied on a constitutive CD19 level below the threshold of CAR activation, combined with the ability to drastically increase absolute CD19 levels through the use of PRP-regulated promoters, as seen for P_{MFA2}-CD19 reaching up to 15.3±6.2-fold increased activation of CAR+ Jurkat cells at 0.01 µM relative to the unstimulated condition ($p=0.0007$) (**Suppl. Fig. 10**). Insufficiency to reach the threshold for efficient CAR activation explains why P_{FUS1}-CD19 could only increase activation 3.1±0.2-fold at 1 µM (**Suppl. Fig. 10**), despite containing the processing module promoter (P_{FUS1}) with the highest fold change regulation (**Fig. 3F**).

To confirm the specificity and orthogonality of the SCASA yeast-induced CAR activation, we employed the $CD19^{neg}$ control yeast (P_{PGK1}-Empty), as well as co-cultivation setups with a constant number of Jurkat cells that varied in the proportion of CAR+ cells, spanning from 0-100% CAR+ (**Fig. 4C**). With or without GPCR stimulation, only yeast cells containing CD19 in the display design could significantly increase the activation of CAR+ Jurkat cells; P_{MFA2}-CD19, P_{PGK1}-CD19, P_{TDH3}-CD19, and P_{FUS1}-CD19 ($p<0.0001$) (**Fig. 4B-C**), while the $CD19^{neg}$ control (P_{PGK1}-Empty) never induced detectable Jurkat cell activation under any conditions of 0-100% CAR+ levels (**Fig. 4C**) or GPCR stimulation levels (**Fig. 4B**). Likewise, no significantly activated Jurkat cells were detected in the range of 0-10% CAR+ for any co-cultivation, however, any increase >10% CAR+ provided significantly higher responses for NALM6 and CD19-expressing yeast designs only ($p \leq 0.0331$). SCASA yeast cell-displayed CD19 activated CAR+ Jurkat cells in an antigen density-dependent manner, with each SCASA yeast design providing significantly different CAR activation dynamics in the 0-100% CAR+ range ($p<0.0001$) (**Fig. 4C**) and across GPCR stimulation ($p<0.0001$) (**Fig. 4B**), retaining the same order of activation intensity as their CD19 levels (**Fig. 3D-E**). Hence, NFAT activation of Jurkat cells by SCASA yeast cells was fully dependent

on both surface presentation of CD19 on SCASA yeast cells and expression of CARs in Jurkat cells (**Fig. 4B-C**). We thus conclude that there are no indications that yeast itself activates T cells, at least through NFAT-associated pathways, and can thus be considered an orthogonal "canvas" by which CAR T cell activation is specific to CD19-presentation by SCASA yeast cells and dependent on the density presented thereof.

In summary, CAR T cells (Jurkat NFAT-Luc) were activated by CD19-presenting SCASA yeast cells in a manner that was i) CD19-specific, ii) CAR-specific, iii) CD19 antigen density sensitive in regards to the intensity of NFAT activation, iv) different for each SCASA yeast cell design, v) controllable through GPCR stimulation in the SCASA yeast cells, vi) capable of surpassing activation levels of NALM6 cancer cells, and vii) unaffected by the presence of yeast itself (**Fig. 4B-C**).

Characterizing a donor-derived CAR T cell product using SCASA yeast cells

One important aspect of advancing cellular immunotherapies is the ability to robustly characterize responses of CAR T cell products resulting from novel designs or manufacturing methods. For this purpose, we proceeded to demonstrate the clinical relevance of applying SCASA yeast cells in characterizing a donor-derived CAR T cell product's performance. As a case study, we applied a novel CRISPR-MAD7 method for CAR transgene insertion via electroporation in pan-T cells isolated from a healthy donor [73], to generate an alternative Hu19-CD8α-CD28-CD3ζ CAR T cell product containing fully-human antigen-binding domains [74,75]. The response profiles and population behavior of this CAR T cell product were characterized by flow cytometry after co-cultivation with SCASA yeast cell design P_{PGK1}-CD19 with direct comparison to NALM6 cancer cells at three different cell-to-cell ratios; 0.2x, 1.0x, and 5.0x target cells to 100,000 alive CAR T cells. We included a control (CTRL) T cell culture, established by electroporation of the same T cell isolate but without the CAR construct, as well as the $CD19^{neg}$ control yeast (P_{PGK1}-Empty), to confirm the orthogonality of the SCASA yeast cells (**Fig. 5**).

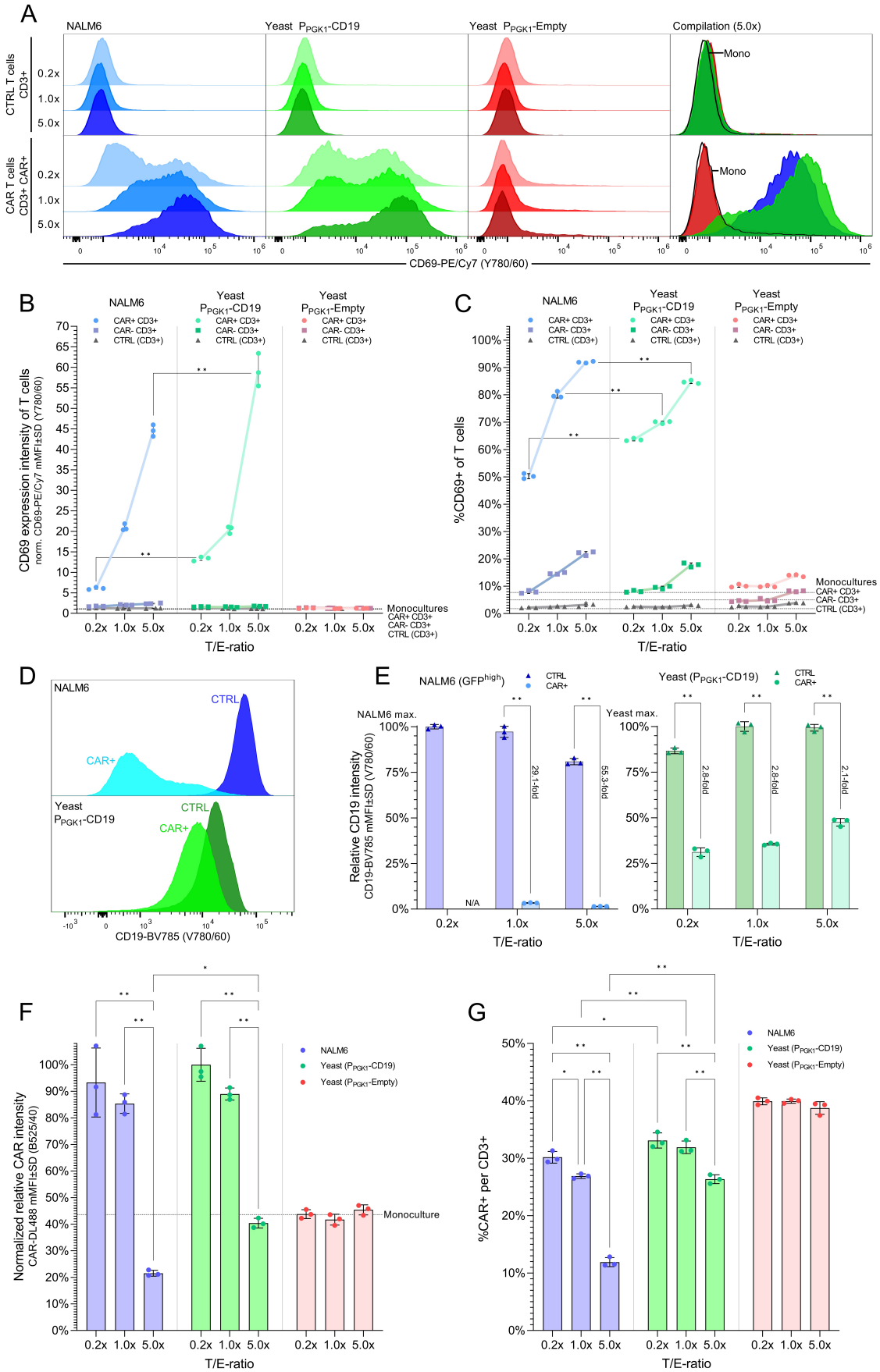
A
NALM6
Yeast PPGK1-CD19
Yeast PPGK1-Empty
Compilation (5.0x)
CTRL T cells CD3+
CAR T cells CD3+ CAR+
0.2x
1.0x
5.0x
Mono
CD69-PE/Cy7 (Y780/60)
B
CD69 expression intensity of T cells
norm. CD69-PE/Cy7 mMFI±SD (Y780/60)
CAR+ CD3+
CAR- CD3+
CTRL (CD3+)
Monocultures
T/E-ratio
C
%CD69+ of T cells
D
CTRL
CAR+
CD19-BV785 (V780/60)
E
NALM6 (GFPhigh)
Yeast (PPGK1-CD19)
NALM6 max.
Yeast max.
Relative CD19 intensity
CD19-BV785 mMFI±SD (V780/60)
N/A
29.1-fold
55.5-fold
2.8-fold
2.1-fold
F
Normalized relative CAR intensity
CAR-DL488 mMFI±SD (B525/40)
Monoculture
G
%CAR+ per CD3+

Figure 5. Activation of CAR T cells from a healthy donor using engineered SCASA yeast cells. A. Expression of activation marker CD69 after co-cultivations of control (CTRL) T cells (alive CD3+ population) (*upper row*) and CAR T cells (alive CD3+ CAR+ population) (*lower row*). CTRL and CAR T cells were co-cultivated with NALM6 (*blue*), SCASA yeast cell P_{PGK1}-CD19 (*green*), and negative control SCASA yeast P_{PGK1}-Empty lacking CD19 (*red*), at three different target-to-effector (T/E) cell ratios (0.2x, 1.0x, and 5.0x) for 20 hrs. The far right column shows an overlay of CD69 T cell responses for 5.0x co-cultivations, at which the dotted line represents unstimulated monocultures (Mono) of the T cells. **B**: CD69 expression intensity of different T cell populations from co-cultivations with target cells: CAR+ (*circle*) and CAR- (*square*) T cells from the CAR-engineered population, and non-engineered CTRL T cells (*triangle*). All have been normalized to CTRL T cell monocultures. Horizontal dotted lines represent baseline CD69 levels of monocultures. **C**: Percentage of T cell populations expressing CD69 (%CD69+) at any intensity for co-cultivations with all target cells. Horizontal dotted lines represent baseline %CD69+ populations of monocultures. **D**: CD19 levels on target cells after co-cultivations at 5.0x ratios of NALM6 (*blue*) and SCASA yeast cell P_{PGK1}-CD19 (*green*) in CAR T cell (*light*) and CTRL T cell (*dark*) cultures. **E**: Relative CD19 levels to the measured maximum of each target cell type individually after co-cultivations with CTRL T cells (*triangle*) and CAR T cells (*circle*). **F**: CAR expression intensity of CAR+ population of engineered cells relative to the CAR- population (background) and normalized to the maximal CAR expression measured. **G**: Percentage of CAR+ T cells per CD3+ T cell detected after co-cultivations. Markers were quantified by flow cytometry. Data represents means of cell counts or median fluorescence intensities (mMFI) for three biological replicates (n=3) and standard deviations hereof. Histograms are normalized to the mode (CD69) or unit area (CD19) and are representative replicates. Significance levels: * P≤0.01, ** P≤0.0001. Not all comparisons are shown. Statistics and extended analyses in: **Suppl. Fig. 11-14** and **Suppl. Table 9**.

SCASA yeast cell P_{PGK1}-CD19 activated the clinical CAR T cell product in a manner that resembled that of cancer cell line NALM6 across all target cell ratios, verifying successful simulation of cancer cells towards the Hu19-CD8α-CD28-CD3ζ CAR T cell product (**Fig. 5A-C**). Specifically, CAR+ CD3+ T cells showed up-regulation of activation marker CD69 in co-cultures for all target cell ratios with SCASA yeast cell P_{PGK1}-CD19 ($p<0.0001$) and NALM6 ($p\leq0.0001$), while no CAR- CD3+ T cells were activated for any target cell or condition, as also seen for the non-engineered CTRL T cells (**Fig. 5A-B**). In addition, activation of donor-derived CAR T cells using SCASA yeast cells was detected for additional SCASA yeast cell designs (P_{MFA2}-CD19 and P_{TDH3}-CD19), through up-regulation of both activation markers CD69 and CD25, and was possible immediately after cell product manufacturing and re-confirmed after 5 months of cryopreservation in liquid nitrogen (**Fig. 5, Suppl. Fig. 11**).

In summary, only T cells with successful CAR insertion by the CRISPR-MAD7 method were activated, which could be verified with both NALM6 cancer cells and SCASA yeast cells. Lastly, T cell activation was conditionally dependent on the expression of CARs (**Fig. 5A-B**).

SCASA yeast cells are efficient and robust CAR T cell activators

Having confirmed that CAR T cell products could be verified with SCASA yeast, we next sought to investigate the efficiency and robustness of the activation. Here, we found that increasing the ratio of SCASA yeast cells per CAR T cell intensified CAR activation, with significantly increased CD69

expression levels per CAR T cell, rising from 13.3±0.5-fold to 59.2±4.0-fold the level of CTRL T cells ($p<0.0001$)(**Fig. 5B**), as well as enlargement of the population of activated CAR T cells (%CD69+) from 63.6±0.5% to 84.7±0.6% ($p<0.0001$)(**Fig. 5C**). A similar behavior was seen for the response to NALM6 at increasing ratios, however with significant differences to SCASA yeast, as NALM6 provided lower or equal intensity of CAR activation, spanning from 6.1±0.3-fold to 44.6±1.4-fold CD69 expression ($p<0.0001$)(**Fig. 5B**), and had a larger spread in the number of activated CAR T cells, spanning from 50.3±0.9% to 91.9±0.3% ($p<0.0001$)(**Fig. 5C**). Overall, functional antigen recognition and activation of the CAR T cell product could be verified both using SCASA yeast and NALM6, with a shared conclusion that CAR T cells are activated in a cell-to-cell ratio-dependent manner in relation to the amount of activated CAR T cells and their response intensity.

Interestingly, P_{PGK1}-CD19 SCASA yeast cells could activate CAR T cells more intensely than NALM6 (**Fig. 5B**), yet had a CD19 density of merely 23.35±1.65% compared to that of NALM6 (**Suppl. Fig. 12**), which led us to investigate the target cells' performance and robustness throughout co-cultivation. Here, we discovered that NALM6 CD19 levels were highly unstable throughout co-cultivation, evidenced by the occurrence of a CAR T cell-resistant $CD19^{low}$ relapse-like phenotype of the NALM6 cancer cells during co-cultivation, as reported elsewhere [32,50,51] (**Fig. 5D**). The appearance of the drastic $CD19^{low}$ NALM6 phenotype was fully dependent on the expression of CARs in T cells (SV=98.2%, $p<0.0001$) (**Suppl. Table 9**), and developed only in CAR T cell co-cultivations, while being undetectable in NALM6 monocultures and in co-cultivations with CTRL T cells (**Fig. 5D**). Specifically, NALM6 CD19 levels dropped 98.54±0.05% within 20 hrs of co-cultivation to a level that was 55.4±2.2-fold lower than in the CTRL co-cultivation ($p<0.0001$)(**Fig. 5E**), resulting in a large alive $CD19^{low}$ population (19.8±0.9% of all cells detected) for the 5.0x co-cultivation with CAR T cells (**Suppl. Fig. 13**). When equal amounts of NALM6 and CAR T cells were co-cultivated the effect was less drastic (29.0±1.9-fold lower CD19 levels) (**Fig. 5E**), resulting in killing of most NALM6 cells (0.5±0.1% of all cells detected) (**Suppl. Fig. 13**). When CAR T cells were in excess, all NALM6 cells were killed (**Suppl. Fig. 13**). Comparatively, SCASA yeast cells showed a more robust CD19 density than NALM6 throughout co-cultivations (**Fig. 5D**), with only 2.1±0.1-fold to 2.8±0.1-fold differences in CD19 levels between CTRL and CAR T cell co-cultivations (**Fig. 5E**). Additionally, CD19+ SCASA yeast cell numbers were up to 17.0-fold more robustly maintained during CAR T cell co-cultivations than NALM6 ($p<0.0001$) (**Suppl. Fig. 14**), and there was no clear indication that SCASA yeast cells were killed by the CAR T cell cytotoxic response, contrary to NALM6 (**Suppl. Fig. 13**). Hence, the difference in CAR T cell activation patterns could be explained by a higher robustness in both antigen density and cell numbers of SCASA yeast cells compared to NALM6, allowing for a more consistent target cell population to continuously provide activation signals to the CAR T cells.

Upon further inspection of the CAR T cells, it became evident that both CAR expression patterns and the amount of CAR+ cells per CD3+ T cells were alternating throughout co-cultivation in a CD19-dependent manner. CAR expression was elevated at low and equal target-to-effector cell ratios ($p<0.0001$), while target cell outnumbering of CAR T cells was associated with lower CAR expression intensities ($p<0.0001$)(**Fig. 5F**). This antigen-dependent up- and down-modulation of CAR surface levels has previously been shown to be dependent on CAR stimulation levels, and reported to be caused by at least CAR expression regulation and CAR internalization [32,34,41,50,76]. The % CAR+ of CD3+ T cells dropped with an increase in target cell numbers ($p<0.0001$), indicating a loss of CAR+ T cells (**Fig. 5G**). Importantly, these effects were seen for both SCASA yeast cells and NALM6, but in both cases more drastic for NALM6 (**Fig. 5F-G**).

Orthogonality was confirmed by the $CD19^{neg}$ yeast control (P_{PGK1}-Empty) which did not activate CAR T cells or CTRL T cells under any circumstances, showing no increase in CD69 or CD25 (**Fig. 5A-B, Suppl. Fig. 11**), did not affect CAR expression intensity (**Fig. 5F**), or change the number % CAR+ cells per CD3+ cells (**Fig. 5G**), collectively showing that the activation of CAR T cells by SCASA yeast cells was specifically caused by the interaction between surface-displayed CD19 and successfully expressed CARs, and that yeast could not activate CD3+ T cells unspecifically, corroborating the CAR Jurkat NFAT-Luc observations (**Fig. 4**).

In summary, SCASA yeast cells provided an efficient method for activating and confirming functionality of a novel donor-derived CAR T cell product. SCASA yeast cells perform on par with cancer cells in terms of response dynamics, yet with higher robustness and consistency in regards to antigen density and target cell numbers throughout co-cultivation.

Discussion

Enabled by the outstanding engineerability of yeast as a synthetic biology platform, we have shown that the SCASA yeast technology can accomplish controllable interspecies cell-to-cell communication via CD19 signal presentation at intensities spanning >3 orders of magnitude in fold changes, in a robust and gradual (non-binary) manner, dependent on GPCR stimulation of yeast cells (**Fig. 3**). Based on this, we have shown that SCASA yeast cells can simulate cellular interactions of CD19+ cancer cells and control the activational state of CAR T cells in a manner that is dependent on both antigen density and cell-to-cell ratios, exemplified by the activation of two different CARs, FMC63-CD8α-4-1BB-CD3ζ and Hu19-CD8α-CD28-CD3ζ, detected by up-regulation of CD69 and CD25 markers, as well as increased NFAT activity (**Fig. 4-5, Suppl. Fig. 11**). The SCASA platform development has also provided novel insight into yeast biology, with for example the characterization of promoter parts for inversion of agonist GPCR responses (P_{HPF1} and P_{CSS1}) of interest to biosensor engineering (**Fig.**

2), and the PRP-induced expression boost, which we envision can be employed to tactically increase expression levels of any protein of interest from any promoter upon PRP stimulation (**Fig. 2-3**).

The application of yeast in immunological research is a developing field, and we envision that advancements in synthetic biology, such as improved sense-response systems and a broader repertoire of yeast-controlled immunoregulators, could expand the yeast toolbox for immunological research. For example, of specific interest to synthetic yeast-based T cell activation, another recent study employing yeast co-cultivations for immunological research, reported specific activation of T cells through displayed peptide antigens presented in major histocompatibility complexes (pMHC) for screening T cell receptor (TCR) interactions [63].

For applications where control and robustness are of importance, such as correlating an immune cell phenotype to the intensity of a specific signal, our results for CAR T cell activation show that a yeast platform can outperform cancer cell lines on certain parameters. We base this on the equal ability to achieve activation phenotypes, combined with higher robustness in sustained signal intensities (e.g. CD19) and cell numbers during co-cultivation, and due to the unprecedented dynamicity of control and greater orthogonality associated with the use of yeast cells (**Fig. 4-5, Suppl. Fig. 9-14**). Specifically, SCASA yeast cells could improve the isolation of responses from distorting natural effects of human cell-to-cell interactions, such as rapid and extensive CAR-dependent NALM6 antigen down-modulation forming a $CD19^{low}$ population [32,50,51], and the cytotoxic sensitivity of NALM6 imposing a selective pressure bias and loss of CD19+ cells (**Fig. 5, Suppl. Fig. 13-14**). Orthogonality can arguably also be regarded as a limitation, as SCASA yeast cells do not simulate the full spectrum of complex interactions, as for example seen between a cancer cell and an immune cell. Hence, we specifically regard the SCASA yeast platform as useful for applications where specific signals must be isolated from the complex interaction network. Additionally, absolute orthogonality is potentially difficult to obtain when employing yeast, as T cells express pattern recognition receptors (PRRs) that can bind *S. cerevisiae* pathogen-associated molecular patterns (PAMPs), such as Toll-like receptor 2 (TLR2) and CD5 recognition of yeast cell wall-derived zymosan, which upon stimulation can modify T cell responses [77–80]. Interestingly, yeast-induced PRR stimulation of T cells might induce relevant phenotypes in relation to cancer immunotherapy, with for example studies showing that TLR2 stimulation can improve T cell anti-cancer phenotypes [81], lower antigen density thresholds for T cell activation [82], and improve CAR T cell responses [83]. The possible impact and extensiveness of T cell PRR engagement by *S. cerevisiae* PAMPs on CAR T cell activation, including differences from NALM6 (**Fig. 4-5**), and the proposed SCASA system applications, is a considerable uncertainty to be addressed in future investigations.

Nevertheless, with the demonstrated potential and engineerability of yeast platforms, as well as recent developments and trends in yeast synthetic biology, we anticipate the advancement of yeast-based systems towards targeting immunological challenges and providing novel applications in the future.

Methods

Molecular cloning for yeast engineering

PCR and DNA handling

Genomic DNA (gDNA) was purified using the Yeast DNA Extraction Kit (Thermo Scientific, Cat.#78870). Custom DNA synthesis was done using gBlocks™ Gene Fragment synthesis service (Integrated DNA Technologies). For amplification of DNA fragments for cloning or genome integration, and inverse PCR plasmid construction, Phusion High-Fidelity (HF) PCR Master Mix with HF Buffer (Thermo Scientific, Cat.#F531L) was used, and, specifically, for amplification of Uracil-Specific Excision Reagent (USER) cloning DNA fragments, Phusion U Hot Start PCR Master Mix (Thermo Scientific, Cat.#F533L) was used with primers with USER-compatible uracil-containing tails. Standard 50 µL PCR reactions were composed of; 25 µL PCR Master Mix (2X), 2 µL of each primer (10 µM), DNA template scaled to 100-200 ng gDNA or 10-20 ng plasmid DNA, and Milli-Q H_2O to a total reaction volume of 50 µL. For diagnostic and genotyping PCRs, such as colony PCR of *Escherichia coli* or yeast, One*Taq*® Quick-Load® 2X Master Mix with Standard Buffer (New England BioLabs, Cat.#M0486) was used. For each *E. coli* colony PCR, a 10 µL PCR mix was made; a small amount of cell mass was added to a mix of 5 µL PCR Master Mix (2X), 1 µL of each primer (10 µM), and 3 µL Milli-Q H_2O. For each yeast colony PCR, a 20 µL PCR mix was made; cell mass was added until visible turbidity in a mix of 1 µL of each primer (10 µM) and 8 µL Milli-Q H_2O, followed by cell lysis by heating at 98°C for 15 min., and after cooling, 10 µL PCR Master Mix (2X) was added. PCRs were conducted according to the manufacturer's protocols using an S1000 Thermal Cycler (Bio-Rad). All primers were synthesized using a Custom DNA Oligos service (Integrated DNA Technologies) and can be found in **Suppl. Table 10**. Gel electrophoresis was done in 1%w/v agarose gels of 1X Tris-acetate-EDTA buffer at 90v for 30 min., using TriTrack DNA 6X Loading Dye (Thermo Scientific, Cat.#R1161), GeneRuler 1 kb DNA Ladder (Thermo Scientific, Cat.#SM0311), and RedSafe™ Nucleic Acid Staining Solution (iNtRON Biotechnology, Cat.#21141). Gel imaging was conducted on a Gel Doc XR+ System (Bio-Rad). PCR amplicons were purified via gel purification or column purification using the NucleoSpin Gel and PCR Clean-up kit (Macherey-Nagel, Cat.#740609.50). Amplicon sequences were verified by Sanger sequencing using the Overnight Mix2Seq Kit service (Eurofins Genomics). Primers, DNA fragments, amplicons, plasmids, and gDNA

were always dissolved in Milli-Q H_2O and stored at -20°C. An overview of all DNA parts, backbones, and plasmids can be found in **Suppl. Table 11-12.**

Construction of plasmids

Plasmid vectors containing genome-integration expression cassettes were based on the EasyClone-MarkerFree system compatible with CRISPR/Cas9 engineering [84], and were constructed with USER cloning and assembly techniques [85] , however, modified by using custom standardized USER-compatible primer tails for DNA parts and inverse PCR for conversion of USER-compatible backbones, denoted MAD-cloning (**Suppl. Fig. 15**). Linearized USER-ready MAD-cloning backbones were generated by purification of inverse PCR-amplified EasyClone-MarkerFree integrative vectors using primers with USER-compatible tails. Similarly, custom yeast expression plasmids were constructed by converting template expression plasmids [67,86] into MAD-cloning compatible backbones. Employed parts, such as promoters, terminators, protein-coding sequences (CDSs), or entire genes, were amplified from yeast gDNA, plasmids, or ordered as gBlocks™, and in some cases modified by in-frame fusion using USER-cloning, and coding sequences were modified to contain the AAAACA Kozak sequence. Each cassette assembled by MAD-cloning contained standardized interchangeable parts: I) a promoter, II) a CDS, III) a terminator, IV) a linearized backbone, which for genome integration contained homology arms directed at EasyClone-MarkerFree genome integration sites flanked by *Not*I-sites. USER-assembly reactions contained 20-40 ng linearized USER-ready backbone, 40-80 ng of each USER-compatible part, 0.5 µL USER® Enzyme (New England BioLabs, Cat.#M5505), 1 µL 5X Phusion HF Buffer (Thermo Scientific, Cat.#F518L), and Milli-Q H_2O to a total reaction volume of 5 µL. USER-assembly mixes were incubated at 37°C for 30 min. and transformed into *E. coli*. Plasmids for integration of GPCR expression cassettes were assembled as previously described [52]. For CRISPR/Cas9 engineering, all gRNA was expressed from cassettes using the snoRNA *SNR52* promoter and a *SUP4* terminator [87]. Custom yeast gRNA-expression plasmids were generated by inverse PCR of template gRNA-expression plasmids using a 5'-phosphorylated primer and a primer with a tail for replacing the 20 bp gRNA target sequence. Purified amplicons were then blunt-end ligated in a reaction containing: 1 µL T4 DNA Ligase (Thermo Scientific, Cat.#EL0011), 2 µL 10X T4 DNA Ligase Buffer (Thermo Scientific, Cat.#EL0011), and 17 µL amplicon dissolved in Milli-Q H_2O, which was incubated for 2 hrs at room temp. Template plasmid was then removed by addition of 1 µL DpnI (New England BioLabs, Cat.#R0176), 5 µL 10X FastDigest Buffer (Thermo Scientific, Cat.#B64), and 24 µL Milli-Q H_2O, which all was incubated for 1 hr at 37°C, and finally transformed into *E. coli*. All *E. coli* transformants for plasmid assembly were genotyped by colony PCR to screen for successful assembly, and correct assembly was verified by Sanger sequencing of purified plasmids using the Overnight Mix2Seq Kit service (Eurofins

Genomics). Plasmids were purified from *E. coli* cultures using the NucleoSpin Plasmid kit (Macherey-Nagel, Cat.#740588.50). All plasmids contained ampicillin resistance (*ampR*) for propagation in *E. coli*, and retention in yeast relied on auxotrophic markers (*HIS3*, *URA3*, *LEU2*, *TRP1*) or nourseothricin antibiotic resistance (*NatR*). Primers, DNA fragments, amplicons, plasmids, and gDNA were always dissolved in Milli-Q H_2O and stored at -20°C. An overview of parts, backbones, constructed plasmids, and plasmids originating from other studies [52–54,57,58,67,70,71,84,86] can be found in **Suppl. Table 11-12**, and primers in **Suppl. Table 10**.

Repair and Intentional Primer Dimer (IPD) PCR templates for gene knockout or alteration

For direct genome engineering, such as gene knockouts or minor alterations of genome sequences, DNA repair templates were co-transformed with gRNA-plasmids into Cas9-expressing yeast strains. Repair templates were either two genome-amplified sequences with overlapping homology defined by primer tails or an Intentional Primer Dimer (IPD) PCR amplicon with flanking homology to the cut site. IPD-PCR templates were generated by annealing and PCR-amplifying two complementary primers using each other as templates at their predicted annealing temperatures (50 µL Phusion HF, with 4 µL of each primer at 10 µM). IPD-PCR templates had genome-targeting homology tails and contained a complementary binding region for their amplification, which was also composed of one of several genome-unique CRISPR landing pads previously characterized [88], allowing for easy reengineering of the site (**Suppl. Fig. 16**).

Bacterial handling for plasmid construction and propagation

Plasmid propagation and USER-assembly were conducted by heat-shock transformation into *E. coli* strain DH5α, which was cultivated in Terrific Broth or Luria-Bertani with ampicillin (100 mg/L) at 37°C in liquid media at 300 r.p.m. or on agar plates for 16-20 hrs. Before transformation, *E. coli* DH5α was made chemically competent and stored at -80°C until needed [89]. All *E. coli* strains were stored as cryostocks in media with 25% (v/v) glycerol at -80°C.

Yeast strains, media, and engineering

Yeast handling

All yeast strains were engineered from *S. cerevisiae* strain BY4741 (**Suppl. Table 13**). Strains were grown in YPD media with 2% (w/v) glucose except for during experiments or for plasmid retention, in which strains were grown in Synthetic Complete (SC) media with 2% (w/v) glucose using appropriate amino acid dropout mixes (Sigma-Aldrich) and/or with the addition of antibiotic nourseothricin (100 mg/L) (Jena Bioscience, Cat.#AB-101). For experiments requiring pH-control, a SC

medium with ammonium sulfate (AS) and urea (SC-AS/Urea) was buffered using citrate-phosphate buffer (CPB) [90]. Yeast strains were generally grown at 30°C at 250 r.p.m. or on 2% (w/v) agar plates, unless otherwise stated for specific experiments. All strains were stored as cryostocks in media with 25% (v/v) glycerol at -80°C.

Yeast transformation and engineering

All transformations of yeast were done using the LiAc/ssDNA/PEG method [91]. Plasmid-based expression utilized either 2µ- or CEN/ARS-type plasmids. All genome engineering relied on CRISPR/Cas9-based methods, by having cells constitutively expressing Cas9 from pEDJ391 [86]. Genome integrations relied on co-transformation of I) FastDigest™ *Not*I-linearized (Thermo Fisher, Cat.#FD0593) cassette-containing USER-assembled plasmids with homology arms and II) gRNA helper vectors, both targeting the characterized integration sites described for the EasyClone MarkerFree system [84]. Gene knockouts relied on co-transformation of I) a gRNA expression vector targeting the site of interest and II) an IPD-PCR repair template with homology flanking the Cas9 cut site, which contained a genome-unique CRISPR landing pad for enabling reengineering of the site [88]. Similarly, scarless gene alterations were done by using an IPD-PCR template containing the novel sequence of interest. Genomic engineering was confirmed by genotyping via colony PCR and Sanger sequencing of cassettes, as described above.

From the BY4741 background, the strain DIX14 was optimized for GPCR biosensing by overexpression of native α-factor pheromone-sensing mating GPCR Ste2 (P_{CCW12}-*STE2*-T_{CYC1}), and by balanced expression of native G protein G_α-subunit (P_{PGK1}-*GPA1*-T_{CYC1}), as well as by deletion of native PRP-coupled GPCRs (*ste2Δ0* and *ste3Δ0*), native G_α-subunit (*gpa1Δ0*), a negative feedback regulator (*sst2Δ0*), an α-factor protease (*bar1Δ0*), and a cyclin-dependent kinase inhibitor that induce G1 cell cycle arrest (*far1Δ0*). Furthermore, native *AGA2* was deleted in preparation for YSD optimization (*aga2Δ0*). From DIX14, DIX17-28 were created by integration of yEGFP-expression cassettes. DIX34 was created by knocking out the PRP transcription factor Ste12 (*ste12Δ0*) and integrating a LexA-based synthetic transcription factor, as well as a yEGFP cassette with a LexO-containing promoter for orthogonalized signaling. The strain DIX41 was optimized for YSD by Aga1 overexpression (P_{TDH3}-*AGA1*-T_{ADH1}). DIX44-56,74 strains were generated from DIX41 for CD19 YSD experiments and co-cultivations, by integration of CD19-expression cassettes. Based on DIX45, genome alterations were made to replace the Gpa1 G_α-subunit with $G_{\alpha z}$- and $G_{\alpha i2}$-chimeras, to generate DIX57 and DIX58, respectively, for allowing coupling of heterologous GPCRs. From these strains, heterologous GPCRs were integrated to make the GPCR strain library (DIX59-DIX65). An overview of strains can be found in **Suppl. Table 13**.

Human cell engineering and cultivation

Construction of anti-CD19 CAR Jurkat NFAT-Luc cell line

To investigate the activation of CAR T cells, a Jurkat cell line equipped with a nuclear factor of activated T cell (NFAT) transcription factor luciferase reporter system (Jurkat NFAT-Luc) (Nordic BioSite, Cat.#BPS-60621) was further modified by insertion of an anti-CD19 CAR (FMC63-CD8α-4-1BB-CD3ζ) [72], hence providing a bioluminescent luciferin signal of an intensity proportional to the level of T cell activation. Lentiviral particles containing the CD19 CAR element were produced by lipofectamine-based co-transfection of HEK293 cells with 3rd generation packaging plasmids pMD2.G (Addgene, #12259), pMDLg/pRRE (Addgene, #12251), pRSV-Rev (Addgene, #12253), and the CAR transfer vector (pDTU), a modified version of pLenti-puro (Addgene, #39481), optimized to include a cPPT-CTS sequence, the EF-1α promoter, and a Woodchuck Hepatitis Virus (WHV) Post-transcriptional Regulatory Element (WPRE). 24 hrs after transfection, lentiviral particles were harvested and concentrated using Lenti-X concentrator (Takara Bio) and stored at -80°C. Jurkat NFAT-Luc cells were transduced with lentivirus at an MOI of 5. After transduction, anti-CD19 CAR+ Jurkat NFAT-Luc cells were single-cell sorted and expanded to adequate numbers before cryopreservation in liquid nitrogen. Jurkat cell lines were cultured in RPMI 1640 medium (ATCC modification) (Thermo Fisher, Cat.#A1049101) with 10% fetal bovine serum and 1%pen-strep (RPMI+10%FBS+1%PS) at 37°C with 5% CO_2.

NALM6 cancer cell line

The human CD19+ NALM6 B cell precursor leukemia cell line (DSMZ, no.: ACC 128) was included as a benchmark positive control. NALM6 was cultured in RPMI+10%FBS+1%PS at 37°C with 5% CO_2. The cell line was further engineered by genomic insertion of a CAG-promoter driven GFP-cassette in safe-harbor site AAVS1 using CRISPR-MAD7, as previously described [73].

Isolation of T cells from peripheral blood and CRISPR-MAD7 engineering for CAR insertion

This study was carried out in accordance with the Declaration of Helsinki. Human peripheral blood was obtained from healthy adults after obtaining informed consent (Technical University of Denmark - Rigshospitalet National Hospital approval BC-40). All T cells were derived from the blood of healthy donors collected at the central blood bank at Rigshospitalet (Copenhagen, Denmark). Peripheral blood mononuclear cells (PBMCs) were isolated from buffy coat, by blood filtration using a Falcon 70 µM Cell Strainer (Corning, Cat.#352350), followed by 2X dilution in Dulbecco's Phosphate Buffered Saline with 2% Fetal Bovine Serum (Stemcell Technologies, Cat.#07905), and finally, density centrifugation using SepMate™-50 (IVD) tubes (Stemcell Technologies, Cat.#85460) and Lymphoprep™ (Stemcell Technologies, Cat.#07811), according to the manufacturer's protocols. Pan T

cells were isolated from PBMCs by negative selection, using the EasySep™ Human T Cell Isolation Kit (Stemcell Technologies, Cat.#17951), with EasySep™ Buffer (Cat.#20144) and EasySep™ Magnet, The "big Easy" magnet (Stemcell Technologies, Cat.#18001), according to manufacturer's protocols. T cells were then resuspended at 1×10^6 cells/mL in ImmunoCult™-XF T Cell Expansion Medium (Stemcell Technologies, Cat.#10981) supplemented with Human Recombinant IL-2 (12.5 ng/mL) (Stemcell Technologies, Cat.#78036), IL-7 (5 ng/mL) (Stemcell Technologies, Cat.#78053), IL-15 (5 ng/mL) (Stemcell Technologies, Cat.#78031), and ImmunoCult™ Human CD3/CD28/CD2 T Cell Activator (25 µL/mL) (Stemcell Technologies, Cat.#10990) and cultured for 1.5 days at 37°C with 5% CO_2. After activation, T cells were engineered using CRISPR-MAD7 according to a recently published method,[73] to insert the CAR Hu19-CD8α-CD28-CD3ζ (Hu19-CD828Z), containing an anti-CD19 fully-human scFv (Hu19), CD8α hinge and transmembrane domains, a CD28 costimulatory domain, and a CD3ζ activation domain [74] (Clinical trial: NCT02659943). In addition, the CAR contained a myc-tag for the detection of surface expression. The CAR was expressed using the EF-1α promoter and a bovine growth hormone polyadenylation (bgh-PolyA) signal from the AAVS1 safe-harbor site. The CRISPR-MAD7 crRNA ribonucleoprotein formulation, Hu19-CD8α-CD28-CD3ζ homology-directed repair (HDR) template generation, and transfection of donor-derived (primary) T cells using a Lonza 4D-Nucleofector with shuttle unit with use of M3814 (Selleckchem) recovery followed the previously described methods[73]. Along with the CAR T cells, a control (CTRL) T cell product was established from the same T cell isolate, however without using a CAR HDR template. The CAR T cell product was cultivated in RPMI+10%FBS+1%PS at 37°C with 5% CO_2 for experiments and cryopreserved as 10×10^6 cells/mL in 1 mL 90% heat-inactivated Human AB Serum (Sigma-Aldrich, Cat.#H4522) +10% DMSO in liquid nitrogen. T cells for investigation of viability during co-culture with yeast were obtained from PBMCs isolated from healthy donor buffy coats, by density centrifugation using LymphoPrep™ Solution (Axis-Shield PoC, Cat.#1858) and cryopreserved at −150°C in FBS+10% DMSO. T cells were isolated from PBMCs by negative selection, using the EasySep™ Human T Cell Isolation Kit (Stemcell Technologies, Cat.#17951).

Experimental procedures

Flow cytometry

Flow cytometric measurements were carried out using either a NovoCyte Quanteon 4025 Flow Cytometer System with a NovoSampler Q System (Agilent) or a CytoFLEX-S (V-B-Y-R) instrument (Beckman Coulter), according to the manufacturers' protocols. Specifications are provided in the description of individual experiments below. Gating and compensation were done using FlowJo™ v10.8.1 Software (BD Life Sciences). Gating strategies employed fluorescence minus one (FMO)

controls, as well as the employment of negative controls, where possible, for determining true positive signals (e.g. yEGFP+, CAR+) (**Suppl. Fig. 18-19**).

Processing module promoter characterization

For processing module promoter characterization, a transcriptome analysis was conducted (**Suppl. Fig.1, Suppl. Table 1**), as described previously [52], from which candidate promoters were chosen. Each promoter was defined as the 1,000 bp sequence upstream of the gene CDS, and USER-assembled with yEGFP and T_{CPS1}, to form reporter cassettes. Dose-response and phenotype features of strains containing the selected promoters, P_{MFA2}, P_{FUS1}, P_{AGA2}, P_{FIG1}, P_{MFA1}, $P_{YCL076W}$, P_{HPF1}, P_{IME4}, P_{CSS1}, P_{TDH3}, P_{PGK1} and $P_{6xLexOLEU2}$, were then investigated upon GPCR stimulation via yEGFP expression (**Fig. 2, Suppl. Fig. 2-5**). The yeast strains were inoculated and pre-cultivated in 0.5 mL SC (24 hrs., 30°C, 250 r.p.m.), then diluted 10-fold and further cultivated in SC (24 hrs., 30°C, 250 r.p.m.), whereafter, for each replicate, cultures were diluted 50-fold by transfer to 200 µL volumes comprising a 10-fold dilution series of α-factor (0-100 µM) (peptide-seq.: WHWLQLKPGQPMY) (GenScript) in SC+1%DMSO, and then stimulated for 5 hrs. (30°C, 250 r.p.m.) (**Suppl. Fig. 17**). Flow cytometric measurement was done using a NovoCyte Quanteon flow cytometer (Agilent), with cells suspended in 1X phosphate-buffered saline (PBS), and collection of 20,000 cells per replicate to quantify yEGFP levels (B525/45-A) and PRP-regulated morphological changes (shmooing) (SSC-A). The gating strategy is described in **Suppl. Fig. 18**. Each condition was examined in three biological replicates. A two-way ANOVA with Tukey's or Dunnett's multiple comparisons test was conducted for individual conditions, and to fulfill the assumptions of parametric tests, some data was log_{10}-transformed, all specified in **Suppl. Table 2-3**. Linear and non-linear variable slope (four parameter) regressions can be found in **Suppl. Table 3-4**.

CD19 display characterization

To investigate the different variants of CD19 modules (**Fig. 3, Suppl. Fig. 7-8**), yeast cells were grown and stimulated to present CD19 differentially, whereafter they were stained with antibodies and assessed by flow cytometry. For the investigation of the strain library with constitutive and dynamically regulated expression of CD19 (No YSD, P_{PGK1}-Empty, P_{MFA2}-CD19, P_{FUS1}-CD19, P_{FIG1}-CD19, P_{MFA1}-CD19, P_{HPF1}-CD19, P_{TDH3}-CD19, P_{PGK1}-CD19) strains were inoculated and pre-cultivated in 0.5 mL SC (24 hrs., 30°C, 250 r.p.m.), then diluted 10-fold and further cultivated in SC (24 hrs., 30°C, 250 r.p.m.), whereafter, for each replicate, 50,000 cells were transferred to 300 µL volumes comprising a 10-fold dilution series of α-factor (0-100 µM) (GenScript) dissolved in SC+1%DMSO, and stimulated for 20 hrs. (30°C, 250 r.p.m.). For conventional YSD using strain EBY100 and pCT-plasmid-based expression [67] (**Fig. 3**), strains were pre-cultivated in SC -trp, then transferred to 5 mL SC -trp +2%Gal for induction

of YSD or +2%Gluc as a negative control (24 hrs., 30°C, 250 r.p.m.). For the investigation of P_{GAL1}-titratability of plasmid-based (DIX41+pMAD58) and genome-integrated CD19 YSD (DIX74) (**Suppl. Fig. 6**), strains were pre-cultivated in SC -ura and SC, respectively, then transferred to SC -ura and SC, respectively, with varying concentrations of galactose (0.0002%-2%Gal), using raffinose as compensating carbon source, and YSD was induced for 24 hrs (30°C, 250 r.p.m.). Strains were similarly grown in 2%Gluc as negative controls. For assessment of the GPCR library for inducing CD19 YSD using different types of ligands (**Fig. 3, Suppl. Fig. 8**), strains were pre-cultivated in 0.5 mL SC (24 hrs., 30°C, 250 r.p.m.), then diluted 10-fold and further cultivated in SC (24 hrs., 30°C, 250 r.p.m.), whereafter, for each replicate, 50,000 cells were transferred to 300 µL volumes comprising a dilution series of respective ligands dissolved in pH-buffered SC-AS/Urea medium[90], and stimulated for 20 hrs. (30°C, 250 r.p.m.). DIX45 (Ste2) and DIX59 (No GPCR) was stimulated at pH=5 with 0 µM, 0.01 µM, and 1 µM α-factor (GenScript), DIX60 (Mam2) at pH=5 with 0 µM, 1 µM, and 10 µM P-factor (peptide-seq.: TYADFLRAYQSWNTFVNPDRPNL) (GenScript), DIX61 (MTNR1A) at pH=5 with 0 µM, 1 µM, and 10 µM melatonin (Sigma-Aldrich, Cat.#M5250), DIX62 (ADORA2B) at pH=7 with 0 µM, 0.01 µM, and 1 µM adenosine (Sigma-Aldrich, Cat.#01890), DIX63 (ADRA2A) at pH=7 with 0 µM, 1 µM, and 10 µM clonidine hydrochloride (adrenaline agonist) (Sigma-Aldrich, Cat.#C7897), DIX64 (5HT4b) at pH=5 with 0 µM, 1 µM, and 10 µM serotonin hydrochloride (Sigma-Aldrich, Cat.#H9523), and DIX65 (CXCR4a) at pH=7 by 0 µM, 100 µM, and 1000 µM NUCC-390 hydrochloride (CXCL12 agonist) (Cayman Chemical Company, Cat.#30957).

For yeast cell staining, approx. 500,000 cells were pelleted (800g, 3 min., 5°C), washed twice in 150 µL ice-cold PBSA (1X PBS with 1 g/L bovine serum albumin (Sigma-Aldrich, Cat.#A4503)), then resuspended and incubated in 50 µL primary antibody mix (darkness, 30 min., on ice, 200 r.p.m.). Hereafter, the procedure was repeated for the secondary antibody mix. Finally, cells were pelleted and washed twice in 150 µL ice-cold PBSA, whereafter they were resuspended in 150 µL ice-cold PBSA for flow cytometry using a NovoCyte Quanteon flow cytometer (Agilent). The CD19 epitope was stained with 2.5 µg/mL (1:200) mouse anti-CD19 (FMC63) (Absolute Antibody, Cat.#Ab00613) and 40 µg/mL (1:50) goat anti-mouse-AF647 (polyclonal) (Thermo Fisher, Cat.#A-21236), detected in R667/30-H, and the HA-tag was stained with 2.5 µg/mL (1:400) rabbit anti-HA (RM305) (Thermo Fisher, Cat.#MA5-27915) and 10 µg/mL (1:200) goat anti-rabbit-AF488 (polyclonal) (Thermo Fisher, Cat.#A-11008), detected in B525/45-H. NALM6 was stained analogously for direct comparison of CD19 levels. The gating strategy is described in **Suppl. Fig. 18**. Each condition was examined in three biological replicates and 50,000 cells were sampled per replicate. A one-way or two-way ANOVA with Tukey's, Dunnett's, or Šídák's multiple comparisons test was conducted for the individual conditions,

and to fulfill the assumptions of parametric tests, some data was log_{10}-transformed, all specified in **Suppl. Table 5-6**.

Yeast growth assays in mammalian media

For yeast growth assays (**Suppl. Fig. 9**), strains were seeded at 40,000 cells in 200 µL media and grown at 37°C for 24 hrs in yeast media; SC and pH=5-buffered SC-AS/Urea [90], as well as in human immune cell media; RPMI+10%FBS+1%PS and ImmunoCult™-XF T Cell Expansion Medium. Yeast cells were grown in a BioTek Epoch 2 (Agilent) microplate reader to monitor growth at OD_{630} in three biological replicates.

T cell viability and proliferation in yeast co-cultivations

For assessing T cell viability and proliferation, as well as yeast biosensing during long-term co-cultivation (**Suppl. Fig. 9**), T cells separated from a donor-derived isolate of PBMCs were co-cultured with a yeast strain equipped with Ste2 and a P_{FUS1}-yEGFP cassette (B525/45-A). For co-cultivation, a constant cell number of 500,000 T cells was supplied with ratios of 0.5x (250,000), 1.0x (500,000), or 10x (5,000,000) yeast cells and cultivated in 500 µL RPMI+10%FBS, for each replicate, at 37°C with 5% CO_2 for 4 days (96 hrs). In addition, the 1.0x co-cultures were assessed with supplementation of 20 µM α-factor (GenScript). Yeast was pre-cultivated in 0.5 mL SC (24 hrs., 30°C, 250 r.p.m.), then diluted 10-fold and further cultivated in SC (24 hrs., 30°C, 250 r.p.m.), and then washed two times in 1X PBS before establishing co-cultures (**Suppl. Fig. 17**). T cells were labeled using a CellTrace™ CFSE Cell Proliferation Kit (Thermo Fisher, Cat.#C34554) (B525/45-A) according to the manufacturer's protocol before co-culture establishment, and after co-cultivation the entire culture was stained with anti-CD3-BV421 (1:50) (BD Biosciences, Cat.#562426) (V445/45-A), and using a Fixable Near-IR Dead Cell Stain Kit (Thermo Fisher, Cat.#L34975) (R780/60-A) according to the manufacturer's protocol for assessing T cell viability. For staining, the co-cultures were pelleted (300g, 5 min., 5°C), then washed with 100 µL Cell Staining Buffer (BioLegend, Cat.#420201), whereafter each replicate was resuspended in 50 µL staining mix and incubated (darkness, 30 min., on ice). Then cells were pelleted (300g, 5 min., 5°C), washed with 150 µL ice-cold Cell Staining Buffer, and then resuspended in 150 µL ice-cold Cell Staining Buffer for flow cytometry. The co-cultures were examined in three biological replicates and 50,000 cells were sampled per replicate at day 1 (0 hrs), day 2 (24 hrs), and day 5 (96 hrs) by flow cytometry using a NovoCyte Quanteon flow cytometer (Agilent). The gating strategy is described in **Suppl. Fig. 18**. A two-way ANOVA with Tukey's multiple comparisons test was conducted for the individual conditions, and to fulfill the assumptions of parametric tests, some data was log_{10}-transformed, all specified in **Suppl. Table 7**.

CAR Jurkat NFAT-Luc activation assay with SCASA yeast cells and NALM6

For the investigation of SCASA yeast cell activation of CAR Jurkat NFAT-Luc cells with comparison to NALM6 (**Fig. 4, Suppl. Fig. 10**), several co-cultures were set up. Yeast strains were inoculated and pre-cultivated in 0.5 mL SC (24 hrs., 30°C, 250 r.p.m.), then diluted 10-fold and further cultivated (24 hrs., 30°C, 250 r.p.m.), whereafter for GPCR stimulation, for each replicate, cultures were diluted 50-fold by transfer to 200 µL volumes comprising a 10-fold dilution series of α-factor (0-1 µM) (GenScript) in SC+1%DMSO, and then stimulated for 20 hrs. to induce differential CD19 YSD (30°C, 250 r.p.m.). Before establishment of co-cultures, SCASA yeast cells were pelleted (800g, 3 min.), washed twice in 150 µL PBS, and resuspended in RPMI+10%FBS+1%PS. For the establishment of 0-100% CAR+ Jurkat NFAT-Luc cultures, 0% CAR+ and 100% CAR+ Jurkat NFAT-Luc cultures were titrated by cell counting to control the amount of CAR+ cells in each culture. Then, for each replicate of co-cultures, 200,000 alive Jurkat NFAT-Luc cells were co-cultured with 40,000 target cells (i.e. SCASA yeast cells or NALM6) for 18 hrs in 200 µL RPMI+10%FBS+1%PS at 37°C with 5% CO_2 (**Suppl. Fig. 17**). After co-cultivation, cells were lysed using Pierce™ Luciferase Cell Lysis Buffer (Thermo Fisher, Cat.#16189) and the luciferase activity was examined using the Luciferase Assay System (Promega, Cat.#E1500) according to the manufacturers' protocols. Three replicates were made for each tested condition. Relative activation of Jurkat NFAT-Luc cells was calculated by subtraction of background luminescence and normalization to a 100% CAR+ Jurkat cell mono-culture. A one-way or two-way ANOVA with Tukey's or Dunnett's multiple comparisons test was conducted for the individual conditions, and to fulfill the assumptions of parametric tests, some data was $\log_{10}$-transformed, all specified in **Suppl. Table 8**.

Activation assay of donor-derived CAR T cells with SCASA yeast cells and NALM6

SCASA yeast cell activation of donor-derived CAR T cells was done by co-cultivation with comparison to NALM6 (**Fig. 5, Suppl. Fig. 12-14**). Yeast strains P_{PGK1}-Empty (DIX44) and P_{PGK1}-CD19 (DIX47) were inoculated and pre-cultivated in 0.5 mL SC (24 hrs., 30°C, 250 r.p.m.), then diluted 10-fold and further cultivated (24 hrs., 30°C, 250 r.p.m.). Before the establishment of co-cultures, SCASA yeast cells were pelleted (800g, 3 min.), washed twice in 150 µL PBS, and resuspended in RPMI+10%FBS+1%PS. For co-cultivation, a constant cell number of 100,000 alive CAR+ T cells was supplied with ratios of 0.2x (20,000), 1.0x (100,000), or 5.0x (500,000) SCASA yeast cells or NALM6 cells and cultivated in 200 µL RPMI+10%FBS+1%PS for each replicate. For CTRL T cell co-cultures, the corresponding number of alive T cells was used to maintain the same overall number of T cells. The co-cultures were incubated for 20 hrs at 37°C with 5% CO_2 (**Suppl. Fig. 17**). After co-cultivation, the cultures were stained for flow cytometry using anti-CD69-PE/Cy7 (1:150) (BioLegend, Cat.#310912)

(Y780/60-A), anti-CD3-perCP (1:30) (BioLegend, Cat.#300326) (B690/50-A), anti-c-myc-Dylight488 (1:40) (Abcam, Cat.#ab117499) (B525/40-A), anti-CD19-BV785 (1:50) (BioLegend, Cat.#302240) (V780/60-A), and the Zombie Violet Fixable Viability Kit (BioLegend, Cat.#423114) (V445/45-A) according to the manufacturer's protocol. A master mix was made in Cell Staining Buffer (BioLegend, Cat.#420201). For staining, the co-cultures were first pelleted (300g, 5 min., 5°C) to then carefully aspirate the media, whereafter each replicate was resuspended in 50 µL staining master mix and incubated (darkness, 30 min., on ice). Hereafter, the cells were pelleted (300g, 5 min., 5°C), washed twice with 150 µL ice-cold Cell Staining Buffer, and then resuspended in 100 µL ice-cold Cell Staining Buffer for flow cytometry. Three biological replicates were made for each condition, and measurements were conducted using a CytoFLEX-S (V-B-Y-R) instrument (Beckman Coulter) by analyzing 80 µL of each replicate. The gating strategies are described in **Suppl. Fig. 19**. A one-way, two-way, or three-way ANOVA with Tukey's multiple comparisons test was conducted for the individual conditions, and to fulfill the assumptions of parametric tests, some data was $\log_{10}$-transformed, all specified in **Suppl. Table 9**.

After 5 months of cryopreservation in liquid nitrogen, the CAR T cell product was thawed for reexamination (**Suppl. Fig. 11**). After thawing, the CAR T cells were recovered by two days of cultivation in ImmunoCult™-XF T Cell Expansion Medium (Stemcell Technologies, Cat.#10981) supplemented with Human Recombinant IL-2 (12.5 ng/mL) (Stemcell Technologies, Cat.#78036), with initial seeding at 1×10^6 alive cells/mL. Yeast strains P_{PGK1}-Empty (DIX44), P_{MFA2}-CD19 (DIX48), and P_{TDH3}-CD19 (DIX49) were pre-cultivated with and without stimulation using 0.1 µM α-factor (20 hrs., 30°C, 250 r.p.m.), as described for CD19 display characterization. SCASA yeast cells were pelleted (800g, 3 min.), washed twice in 150 µL PBS, and resuspended in RPMI+10%FBS+1%PS. Co-cultures were then established by combining 75,000 alive CAR+ T cells with 25,000 yeast cells (0.3x) in 200 µL RPMI+10%FBS+1%PS. A positive activation control was made using 1X Leukocyte Activation Cocktail (LAC), with BD GolgiPlug™ (BD Biosciences, Cat.#550583) as positive control. After 20 hrs of cultivation at 37°C with 5% CO_2, cultures were stained for flow cytometry with anti-CD69-PE/Cy7 (1:150) (BioLegend, Cat.#310912) (Y780/60-A), anti-CD25-BB700 (BD Biosciences, Cat.#566448) (B695/40-A), anti-CD3-FITC (BD Biosciences, Cat.#349201) (B525/45-A), and the Zombie Violet Fixable Viability Kit (V445/45-A), as described above. The gating strategies are described in **Suppl. Fig. 19**. Two biological replicates were made for each condition, and measurements were conducted using a NovoCyte Quanteon flow cytometer (Agilent).

Software

Flow cytometry data was analyzed using FlowJo™ v10.8 Software (BD Life Sciences). Statistical analyses and plotting were done using GraphPad Prism v9.4.1 (GraphPad Software). Schematic figure illustrations for **Fig. 1**, **2A**, **3A**, **4A**, and **Suppl. Fig. 16-17**, were created with BioRender.com.

Acknowledgements

This work was supported by the U.S. Department of Energy, grant number DE-SC0018368, to RTG, and the Novo Nordisk Foundation, grant number NNF20CC0035580, to MKJ, and Independent Research Fund Denmark, grant number 0129-00005B, to MO. Authors would like to thank Dr. Jie Zhang for providing plasmids pESC-URA-gRNA_XI-3 and pESC-URA-gRNA_XII-5, as well as Professor Tom Ellis and Dr. William Shaw for plasmid pWS1776.

Author contributions

MD, EDJ, SRH, MO, and MKJ conceived the study. MD led the investigation. MD and NMTK performed yeast characterization experiments. MD designed and constructed all yeast strains and plasmids of this study, except for DIX32-34 and pMAD26,29-30 constructed by NMTK. KR, MD, and GS performed Jurkat NFAT-Luc experiments. RUFW, KR, and MO constructed the CAR Jurkat NFAT-Luc cell line. KZ, MD, and GS constructed donor-derived CAR T cells and performed co-cultivation experiments. MD performed the data analysis. MD, EDJ, and MKJ wrote the manuscript. MKJ, RTG, and MO acquired the funding enabling this research. All authors approved the manuscript.

Ethics declarations

Competing interests

The authors declare the following competing interests: M.D., M.K.J., E.D.J., and G.S. are named as inventors on a pending patent application related to the SCASA technology (EP appl. no.: 23177666.7).

References

1. Cubillos-Ruiz, A. *et al.* Engineering living therapeutics with synthetic biology. *Nat. Rev. Drug Discov.* **20**, 941–960 (2021).
2. Rohaan, M. W., Wilgenhof, S. & Haanen, J. B. A. G. Adoptive cellular therapies: the current landscape. *Virchows Arch.* **474**, 449–461 (2019).
3. June, C. H. & Sadelain, M. Chimeric Antigen Receptor Therapy. *N. Engl. J. Med.* **379**, 64–73 (2018).
4. Sadelain, M., Rivière, I. & Riddell, S. Therapeutic T cell engineering. *Nature* **545**, 423–431 (2017).
5. Cappell, K. M. & Kochenderfer, J. N. Long-term outcomes following CAR T cell therapy: what we know so far. *Nat. Rev. Clin. Oncol.* **20**, 359–371 (2023).
6. June, C. H., O'Connor, R. S., Kawalekar, O. U., Ghassemi, S. & Milone, M. C. CAR T cell immunotherapy for human cancer. *Science* **359**, 1361–1365 (2018).
7. Lee, D. W. *et al.* T cells expressing CD19 chimeric antigen receptors for acute lymphoblastic leukaemia in children and young adults: a phase 1 dose-escalation trial. *Lancet* **385**, 517–528 (2015).
8. Park, J. H. *et al.* Long-Term Follow-up of CD19 CAR Therapy in Acute Lymphoblastic Leukemia. *N. Engl. J. Med.* **378**, 449–459 (2018).
9. Maude, S. L. *et al.* Chimeric antigen receptor T cells for sustained remissions in leukemia. *N. Engl. J. Med.* **371**, 1507–1517 (2014).
10. Maude, S. L. *et al.* Tisagenlecleucel in Children and Young Adults with B-Cell Lymphoblastic Leukemia. *N. Engl. J. Med.* **378**, 439–448 (2018).
11. Si Lim, S. J., Grupp, S. A. & DiNofia, A. M. Tisagenlecleucel for treatment of children and young adults with relapsed/refractory B-cell acute lymphoblastic leukemia. *Pediatr. Blood Cancer* **68**, e29123 (2021).
12. Zhang, X. *et al.* Efficacy and safety of anti-CD19 CAR T-cell therapy in 110 patients with B-cell acute lymphoblastic leukemia with high-risk features. *Blood Adv* **4**, 2325–2338 (2020).

13. Liu, S. *et al.* Which one is better for refractory/relapsed acute B-cell lymphoblastic leukemia: Single-target (CD19) or dual-target (tandem or sequential CD19/CD22) CAR T-cell therapy? *Blood Cancer J.* **13**, 60 (2023).
14. Pasquini, M. C. *et al.* Real-world evidence of tisagenlecleucel for pediatric acute lymphoblastic leukemia and non-Hodgkin lymphoma. *Blood Adv* **4**, 5414–5424 (2020).
15. Schultz, L. M. *et al.* Outcomes After Nonresponse and Relapse Post-Tisagenlecleucel in Children, Adolescents, and Young Adults With B-Cell Acute Lymphoblastic Leukemia. *J. Clin. Oncol.* **41**, 354–363 (2023).
16. Dourthe, M.-E. *et al.* Determinants of CD19-positive vs CD19-negative relapse after tisagenlecleucel for B-cell acute lymphoblastic leukemia. *Leukemia* **35**, 3383–3393 (2021).
17. Sterner, R. C. & Sterner, R. M. CAR-T cell therapy: current limitations and potential strategies. *Blood Cancer J.* **11**, 69 (2021).
18. Nie, Y. *et al.* Mechanisms underlying CD19-positive ALL relapse after anti-CD19 CAR T cell therapy and associated strategies. *Biomark Res* **8**, 18 (2020).
19. Xu, X. *et al.* Mechanisms of Relapse After CD19 CAR T-Cell Therapy for Acute Lymphoblastic Leukemia and Its Prevention and Treatment Strategies. *Front. Immunol.* **10**, 2664 (2019).
20. Bai, Z. *et al.* Single-cell antigen-specific landscape of CAR T infusion product identifies determinants of CD19-positive relapse in patients with ALL. *Sci Adv* **8**, eabj2820 (2022).
21. Majzner, R. G. & Mackall, C. L. Tumor Antigen Escape from CAR T-cell Therapy. *Cancer Discov.* **8**, 1219–1226 (2018).
22. Maude, S. L. *et al.* Sustained remissions with CD19-specific chimeric antigen receptor (CAR)-modified T cells in children with relapsed/refractory ALL. *J. Clin. Orthod.* **34**, 3011–3011 (2016).
23. Lee, D. W., III *et al.* Long-term outcomes following CD19 CAR T cell therapy for B-ALL are superior in patients receiving a fludarabine/cyclophosphamide preparative regimen and post-CAR hematopoietic stem cell transplantation. *Blood* **128**, 218–218 (2016).
24. Gardner, R. A. *et al.* Intent-to-treat leukemia remission by CD19 CAR T cells of defined

formulation and dose in children and young adults. *Blood* **129**, 3322–3331 (2017).

25. Sotillo, E. *et al.* Convergence of Acquired Mutations and Alternative Splicing of CD19 Enables Resistance to CART-19 Immunotherapy. *Cancer Discov.* **5**, 1282–1295 (2015).
26. Orlando, E. J. *et al.* Genetic mechanisms of target antigen loss in CAR19 therapy of acute lymphoblastic leukemia. *Nat. Med.* **24**, 1504–1506 (2018).
27. Fischer, J. *et al.* CD19 Isoforms Enabling Resistance to CART-19 Immunotherapy Are Expressed in B-ALL Patients at Initial Diagnosis. *J. Immunother.* **40**, 187–195 (2017).
28. Braig, F. *et al.* Resistance to anti-CD19/CD3 BiTE in acute lymphoblastic leukemia may be mediated by disrupted CD19 membrane trafficking. *Blood* **129**, 100–104 (2017).
29. Ledererova, A. *et al.* Hypermethylation of CD19 promoter enables antigen-negative escape to CART-19 in vivo and in vitro. *J Immunother Cancer* **9**, (2021).
30. Gardner, R. *et al.* Acquisition of a CD19-negative myeloid phenotype allows immune escape of MLL-rearranged B-ALL from CD19 CAR-T-cell therapy. *Blood* **127**, 2406–2410 (2016).
31. Jacoby, E. *et al.* CD19 CAR immune pressure induces B-precursor acute lymphoblastic leukaemia lineage switch exposing inherent leukaemic plasticity. *Nat. Commun.* **7**, 12320 (2016).
32. Hamieh, M. *et al.* CAR T cell trogocytosis and cooperative killing regulate tumour antigen escape. *Nature* **568**, 112–116 (2019).
33. Fry, T. J. *et al.* CD22-targeted CAR T cells induce remission in B-ALL that is naive or resistant to CD19-targeted CAR immunotherapy. *Nat. Med.* **24**, 20–28 (2018).
34. Walker, A. J. *et al.* Tumor Antigen and Receptor Densities Regulate Efficacy of a Chimeric Antigen Receptor Targeting Anaplastic Lymphoma Kinase. *Mol. Ther.* **25**, 2189–2201 (2017).
35. Hombach, A. A. *et al.* Superior Therapeutic Index in Lymphoma Therapy: CD30(+) CD34(+) Hematopoietic Stem Cells Resist a Chimeric Antigen Receptor T-cell Attack. *Mol. Ther.* **24**, 1423–1434 (2016).
36. Watanabe, K. *et al.* Target antigen density governs the efficacy of anti-CD20-CD28-CD3 ζ chimeric antigen receptor-modified effector CD8+ T cells. *J. Immunol.* **194**, 911–920 (2015).

37. Majzner, R. G. *et al.* Low CD19 Antigen Density Diminishes Efficacy of CD19 CAR T Cells and Can be Overcome By Rational Redesign of CAR Signaling Domains. *Blood* **132**, 963 (2018).

38. Majzner, R. G. *et al.* Tuning the Antigen Density Requirement for CAR T-cell Activity. *Cancer Discov.* **10**, 702–723 (2020).

39. Pillai, V. *et al.* CAR T-cell therapy is effective for CD19-dim B-lymphoblastic leukemia but is impacted by prior blinatumomab therapy. *Blood Adv* **3**, 3539–3549 (2019).

40. Meléndez, A. V. *et al.* Novel lectin-based chimeric antigen receptors target Gb3-positive tumour cells. *Cell. Mol. Life Sci.* **79**, 513 (2022).

41. Burton, J. *et al.* Inefficient exploitation of accessory receptors reduces the sensitivity of chimeric antigen receptors. *Proc. Natl. Acad. Sci. U. S. A.* **120**, e2216352120 (2023).

42. Freyer, C. W. & Porter, D. L. Cytokine release syndrome and neurotoxicity following CAR T-cell therapy for hematologic malignancies. *J. Allergy Clin. Immunol.* **146**, 940–948 (2020).

43. Frey, N. & Porter, D. Cytokine Release Syndrome with Chimeric Antigen Receptor T Cell Therapy. *Biol. Blood Marrow Transplant.* **25**, e123–e127 (2019).

44. Rafiq, S., Hackett, C. S. & Brentjens, R. J. Engineering strategies to overcome the current roadblocks in CAR T cell therapy. *Nat. Rev. Clin. Oncol.* **17**, 147–167 (2020).

45. Li, M. *et al.* The differential effects of tumor burdens on predicting the net benefits of ssCART-19 cell treatment on r/r B-ALL patients. *Sci. Rep.* **12**, 378 (2022).

46. Rotte, A. *et al.* Dose-response correlation for CAR-T cells: a systematic review of clinical studies. *J Immunother Cancer* **10**, (2022).

47. Wang, V., Gauthier, M., Decot, V., Reppel, L. & Bensoussan, D. Systematic Review on CAR-T Cell Clinical Trials Up to 2022: Academic Center Input. *Cancers* **15**, (2023).

48. Hu, Y. *et al.* Antigen-Multimers: Specific, Sensitive, Precise, and Multifunctional High-Avidity CAR-Staining Reagents. *Matter* **4**, 3917–3940 (2021).

49. Zhang, Y. *et al.* Extracellular Vesicles Expressing CD19 Antigen Improve Expansion and Efficacy of CD19-Targeted CAR-T Cells. *Int. J. Nanomedicine* **18**, 49–63 (2023).

50. Blanco, B. *et al.* Overcoming CAR-Mediated CD19 Downmodulation and Leukemia Relapse with T Lymphocytes Secreting Anti-CD19 T-cell Engagers. *Cancer Immunol Res* **10**, 498–511 (2022).

51. Schneider, D. *et al.* A tandem CD19/CD20 CAR lentiviral vector drives on-target and off-target antigen modulation in leukemia cell lines. *J Immunother Cancer* **5**, 42 (2017).

52. Jensen, E. D. *et al.* Engineered cell differentiation and sexual reproduction in probiotic and mating yeasts. *Nat. Commun.* **13**, 6201 (2022).

53. Shaw, W. M. *et al.* Engineering a Model Cell for Rational Tuning of GPCR Signaling. *Cell* **177**, 782–796.e27 (2019).

54. Kapolka, N. J. *et al.* DCyFIR: a high-throughput CRISPR platform for multiplexed G protein-coupled receptor profiling and ligand discovery. *Proc. Natl. Acad. Sci. U. S. A.* **117**, 13117–13126 (2020).

55. Kapolka, N. J. *et al.* Proton-gated coincidence detection is a common feature of GPCR signaling. *Proc. Natl. Acad. Sci. U. S. A.* **118**, (2021).

56. Lengger, B. & Jensen, M. K. Engineering G protein-coupled receptor signalling in yeast for biotechnological and medical purposes. *FEMS Yeast Res.* **20**, (2020).

57. Klesmith, J. R., Wu, L., Lobb, R. R., Rennert, P. D. & Hackel, B. J. Fine Epitope Mapping of the CD19 Extracellular Domain Promotes Design. *Biochemistry* **58**, 4869–4881 (2019).

58. Klesmith, J. R. *et al.* Retargeting CD19 Chimeric Antigen Receptor T Cells via Engineered CD19-Fusion Proteins. *Mol. Pharm.* **16**, 3544–3558 (2019).

59. Boder, E. T. & Wittrup, K. D. Yeast surface display for screening combinatorial polypeptide libraries. *Nat. Biotechnol.* **15**, 553–557 (1997).

60. Roberts, C. J. *et al.* Signaling and circuitry of multiple MAPK pathways revealed by a matrix of global gene expression profiles. *Science* **287**, 873–880 (2000).

61. Reider Apel, A. *et al.* A Cas9-based toolkit to program gene expression in *Saccharomyces cerevisiae*. *Nucleic Acids Res.* **45**, 496–508 (2017).

62. Bean, B. D. M. *et al.* Functional expression of opioid receptors and other human GPCRs in yeast

engineered to produce human sterols. *Nat. Commun.* **13**, 2882 (2022).

63. Wang, L. & Lan, X. Rapid screening of TCR-pMHC interactions by the YAMTAD system. *Cell Discov* **8**, 30 (2022).
64. Younger, D., Berger, S., Baker, D. & Klavins, E. High-throughput characterization of protein–protein interactions by reprogramming yeast mating. *Proceedings of the National Academy of Sciences* **114**, 12166–12171 (2017).
65. Teymennet-Ramírez, K. V., Martínez-Morales, F. & Trejo-Hernández, M. R. Yeast Surface Display System: Strategies for Improvement and Biotechnological Applications. *Front Bioeng Biotechnol* **9**, 794742 (2021).
66. Sun, H. *et al.* Display of heterologous proteins on the Saccharomyces cerevisiae surface display system using a single constitutive expression vector. *Biotechnol. Prog.* **30**, 443–450 (2014).
67. Chao, G. *et al.* Isolating and engineering human antibodies using yeast surface display. *Nat. Protoc.* **1**, 755–768 (2006).
68. Alexander, S. P. H. *et al.* THE CONCISE GUIDE TO PHARMACOLOGY 2019/20: G protein-coupled receptors. *Br. J. Pharmacol.* **176 Suppl 1**, S21–S141 (2019).
69. Hilger, D., Masureel, M. & Kobilka, B. K. Structure and dynamics of GPCR signaling complexes. *Nat. Struct. Mol. Biol.* **25**, 4–12 (2018).
70. Lengger, B. *et al.* Serotonin G Protein-Coupled Receptor-Based Biosensing Modalities in Yeast. *ACS Sens* **7**, 1323–1335 (2022).
71. Wang, Z.-X., Broach, J. R. & Peiper, S. C. Functional expression of CXCR4 in Saccharomyces cerevisiae in the development of powerful tools for the pharmacological characterization of CXCR4. *Methods Mol. Biol.* **332**, 115–127 (2006).
72. Ormhøj, M. *et al.* Chimeric Antigen Receptor T Cells Targeting CD79b Show Efficacy in Lymphoma with or without Cotargeting CD19. *Clin. Cancer Res.* **25**, 7046–7057 (2019).
73. Mohr, M. *et al.* The CRISPR-Cas12a Platform for Accurate Genome Editing, Gene Disruption, and Efficient Transgene Integration in Human Immune Cells. *ACS Synth. Biol.* **12**, 375–389 (2023).

74. Brudno, J. N. *et al.* Author Correction: Safety and feasibility of anti-CD19 CAR T cells with fully human binding domains in patients with B-cell lymphoma. *Nat. Med.* **26**, 803 (2020).

75. Ernst, M. *et al.* Chimeric antigen receptor (CAR) T-cell therapy for people with relapsed or refractory diffuse large B-cell lymphoma. *Cochrane Database Syst. Rev.* **9**, CD013365 (2021).

76. Eyquem, J. *et al.* Targeting a CAR to the TRAC locus with CRISPR/Cas9 enhances tumour rejection. *Nature* **543**, 113–117 (2017).

77. Vera, J. *et al.* The CD5 ectodomain interacts with conserved fungal cell wall components and protects from zymosan-induced septic shock-like syndrome. *Proc. Natl. Acad. Sci. U. S. A.* **106**, 1506–1511 (2009).

78. Sato, M. *et al.* Direct binding of Toll-like receptor 2 to zymosan, and zymosan-induced NF-kappa B activation and TNF-alpha secretion are down-regulated by lung collectin surfactant protein A. *J. Immunol.* **171**, 417–425 (2003).

79. Dunne, M. R., Wagener, J., Loeffler, J., Doherty, D. G. & Rogers, T. R. Unconventional T cells - New players in antifungal immunity. *Clin. Immunol.* **227**, 108734 (2021).

80. Sharma, J., Mudalagiriyappa, S. & Nanjappa, S. G. T cell responses to control fungal infection in an immunological memory lens. *Front. Immunol.* **13**, 905867 (2022).

81. Nouri, Y., Weinkove, R. & Perret, R. T-cell intrinsic Toll-like receptor signaling: implications for cancer immunotherapy and CAR T-cells. *J Immunother Cancer* **9**, (2021).

82. Mercier, B. C., Cottalorda, A., Coupet, C.-A., Marvel, J. & Bonnefoy-Bérard, N. TLR2 engagement on CD8 T cells enables generation of functional memory cells in response to a suboptimal TCR signal. *J. Immunol.* **182**, 1860–1867 (2009).

83. Lai, Y. *et al.* Toll-like receptor 2 costimulation potentiates the antitumor efficacy of CAR T Cells. *Leukemia* **32**, 801–808 (2018).

84. Jessop-Fabre, M. M. *et al.* EasyClone-MarkerFree: A vector toolkit for marker-less integration of genes into Saccharomyces cerevisiae via CRISPR-Cas9. *Biotechnol. J.* **11**, 1110–1117 (2016).

85. Nour-Eldin, H. H., Hansen, B. G., Nørholm, M. H. H., Jensen, J. K. & Halkier, B. A. Advancing

uracil-excision based cloning towards an ideal technique for cloning PCR fragments. *Nucleic Acids Res.* **34**, e122 (2006).

86. Jensen, E. D. *et al.* A synthetic RNA-mediated evolution system in yeast. *Nucleic Acids Res.* **49**, e88 (2021).
87. DiCarlo, J. E. *et al.* Genome engineering in Saccharomyces cerevisiae using CRISPR-Cas systems. *Nucleic Acids Res.* **41**, 4336–4343 (2013).
88. D'Ambrosio, V. *et al.* A FAIR-compliant parts catalogue for genome engineering and expression control in Saccharomyces cerevisiae. *Synth Syst Biotechnol* **7**, 657–663 (2022).
89. Inoue, H., Nojima, H. & Okayama, H. High efficiency transformation of Escherichia coli with plasmids. *Gene* **96**, 23–28 (1990).
90. Prins, R. C. & Billerbeck, S. A buffered media system for yeast batch culture growth. *BMC Microbiol.* **21**, 127 (2021).
91. Gietz, R. D. & Schiestl, R. H. Quick and easy yeast transformation using the LiAc/SS carrier DNA/PEG method. *Nat. Protoc.* **2**, 35–37 (2007).